

N O T I C E

THIS DOCUMENT HAS BEEN REPRODUCED FROM
MICROFICHE. ALTHOUGH IT IS RECOGNIZED THAT
CERTAIN PORTIONS ARE ILLEGIBLE, IT IS BEING RELEASED
IN THE INTEREST OF MAKING AVAILABLE AS MUCH
INFORMATION AS POSSIBLE

DPA



science applications, inc.

(NASA-CR-163901) PHOTOGEOLOGICAL
CONSTRAINTS ON LUNAR AND PLANETARY
VULCANISM, PART 1 Final Report, 7 Dec. 1978
- 7 Dec. 1979 (Planetary Science Inst.)
106 p HC A06/MF A01

N81-16962

Unclas

CSSL 03B G3/91 16959



PHOTOGEOLOGICAL CONSTRAINTS
ON LUNAR & PLANETARY VULCANISM

FINAL REPORT

NAEW-3051

PART 1

Nov. 1979

Planetary Science Institute
Science Applications, Inc.
283 S. Lake Ave.
Pasadena, CA

ABSTRACT

This is an updated Final Report on Tasks 1 and 2 of the program "Photogeological Constraints on Lunar and Planetary Volcanism". Although contract work on this program was completed by Dec. 7, 1978 several materials related to the program were compiled during the subsequent months. As the second year's program under Contract NASW-3051 is now complete (and is being reported on under a separate cover (see Part 2)) it is a propitious time for adding those additional results.

TABLE OF CONTENTS

PART I

TASK 1: Central Volcanic Constructs as Constraints on
the Thermal Evolution and Regional Tectonics
of the Moon and Terrestrial Planets

TASK 2: Origins of Sub-kilometer Lunar Craters: Im-
plications for Mare Basalt Petrogenesis

APPENDICES TO TASKS 1 & 2

PART II

TASK 3: Lava Erosion: Theoretical Concepts and Simple
Analytical Models

TASK 4: Lava Erosion: Laboratory Simulation and Two
Dimensional Finite Element Models

APPENDICES TO TASKS 3 & 4

Task 1: CENTRAL VOLCANIC CONSTRUCTS AS CONSTRAINTS ON
THE THERMAL EVOLUTION AND REGIONAL TECTONICS OF THE
MOON AND TERRESTRIAL PLANETS
(Blasius, Cutts)

1.1 Introduction

Volcanic processes are very significant in lunar and planetary science because of their wide-ranging implications for the composition, internal structure and thermal history of terrestrial bodies. A credible and logical approach to the understanding of volcanic processes is through the investigation of the morphology, distribution, age and tectonic setting of volcanic features by means of photogeologic techniques. The availability of high quality imaging data on bodies other than the Moon and Earth, not only expands our knowledge of those bodies but also provides us with new perspectives with which to approach the study of the Earth and its satellites. In particular, we have an opportunity to recognize what processes are common to many terrestrial bodies and what processes are unique to individual bodies.

In this task we carried out investigations of the morphology, distribution, age and tectonic setting of central volcanic constructs on the Moon, conducted a search for central volcanic constructs on Mercury and studies central volcanic constructs on Mars using new Viking Orbiter data.

1.2 Lunar Volcanic Features

A detailed study was made of lunar domes from geologic maps. The location, mean diameter, elevation, local relief and geological unit identifications of each feature were compiled (Appendix 1.1) and relationships to other domes were indicated. Comparisons were made with another survey of domes (Appendix 1.1) by Head and Gifford (1978). A total of 166 features were recognized in the areas studied.

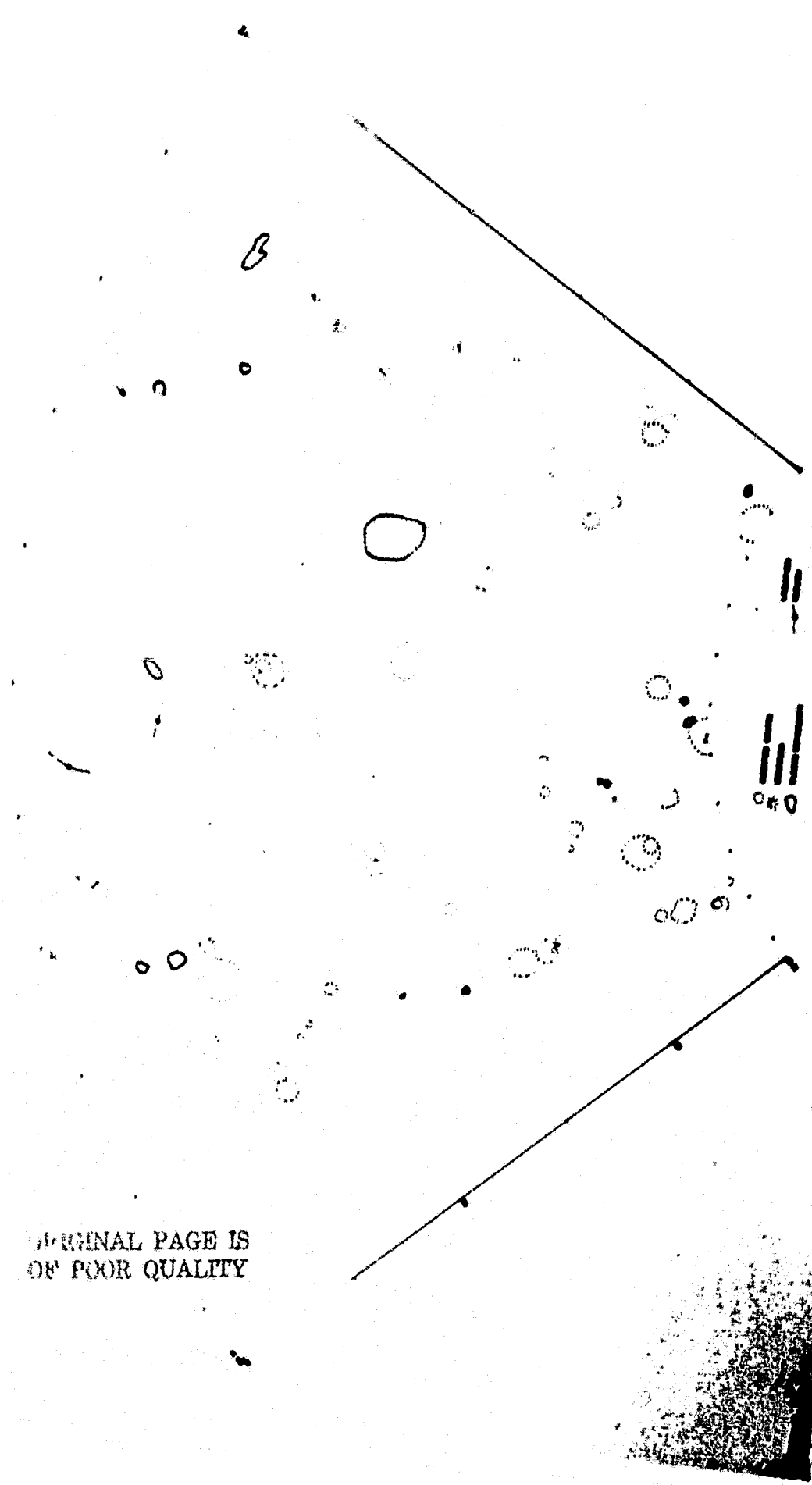
A serious lack of relevant small scale topographic data prevented a meaningful classification of these features. Global radar topographic data have been assembled by Zisk, 1978a,b and Pieters et al., 1978 using methods described by Shapiro et al. (1977). However, the coverage was neither complete enough nor precise enough to provide the data on local relief and slopes that we needed.

1.3 Mercurian Volcanic Features

Studies of a limited set of Mariner 10 stereo image pairs revealed only five examples of non-crater form mountainous features. Locations of these features are mapped in Fig. 1.1. Little independent evidence exists for interpreting these features as volcanic constructs. No relief data were obtained on these features.

ORIGINAL PAGE IS
OF POOR QUALITY

FIGURE 1.1



1.4 Martian Volcanic Constructs

The existence of a suite of well developed volcanic constructs and the availability of extensive Viking Orbiter stereo imaging of these features provided the basis for comprehensive study of these features. This program of investigation began under this program and was continued under the Mars Data Analysis program. Results of these studies are summarized in Blasius and Cutts (1980) (also Appendix 1.1). Other related work on features of Martian volcanoes was reported by Blasius and Cutts, 1978, and by Blasius, 1977.

New topographic maps of six large central volcanoes on Mars were generated. These features are Olympus Mons, Elysium Mons, Albor Tholus, Ceraunius Tholus, Uranus Tholus, and Uranus Patera. Olympus Mons has the general form of a terrestrial basaltic shield constructed almost entirely from lava flows; but with 20 to 23km of relief it is far larger. Flank slopes average about 4° . A nominal density calculated from the shield volume and the local free air gravity anomaly is so high that anomalously dense lithosphere probably underlies the shield.

Uranus Patera is a similar feature of a much lower present relief, about 2km, but its lower flanks have been buried by later lava flood deposits. Elysium Mons has about 13km of local relief and average slopes of 4.4° , not significantly steeper than those of Olympus Mons. Its upper flank slopes are significantly steeper than those of Olympus Mons.

We suggest Elysium Mons is a shield volcano modified and steepened by a terminal phase of mixed volcanic activity. Alternatively, the volcano may be a composite cone.

Albor Tholus is a partially buried 3km-tall shield-like construct. Ceraunius and Uranus Tholus are steeper cone-like features with relief of about 6 and 2km, respectively. Slopes are within the normal range for terrestrial basaltic shields, however, and topographic and morphologic data indicate burial of lower flanks by plains forming lavas. These cones may be lava shield constructs modified by a terminal stage of explosive activity which created striking radial patterns of flank channels.

Differences among these six volcanoes in flank slopes and surface morphology may be primarily consequences of different terminal phases of volcanic activity, which added little to the volume of any construct, and burial of shallow lower flanks by later geologic events.

Topographic data for Olympus Mons, Arsia Mons, and Hadriaca Patera have also been acquired but a complete synthesis of all these data has not been completed. Topographic data has also been compiled by Pike (1978) and formed the base for a morphologic comparison of volcanoes on the inner planets.

CONCLUDING REMARKS

Continuing investigations of volcanic features on the terrestrial planets can provide important constraints on mechanisms of formation of volcanic constructs. At present, research on shields on Mars appears to be most promising; with new data for active volcanoes on the Galilean Io, there is new interest in that body also.

The largest central volcanic constructs, great shields, are of particular interest because their distribution, dimensions and morphologies have been related to the structure and dynamics of planetary interiors. A number of investigators have sought to explain the similar heights and regular spacings of shields on the Earth (e.g., Eaton and Murata, 1960; Ramberg, 1967) and more recently on Mars (Vogt, 1974a; Blasius and Cutts, 1976). Both the Earth and Mars have very large shields, several kilometers in height and extending over tens of thousands of square kilometers. Large shields are certainly absent from the surface of the Moon and our survey indicates no shields on the moon except for low domes seen on lunar maria are shield volcanoes. Large shields are not seen on Mercury; the evidence for small shields based on this study is highly equivocal possibly including small and degraded shields.

The hydrostatic mechanism for raising magma to the point of eruption whether at the summit of a shield or at a fissure source of a plains deposit is particularly pertinent in the comparative study of terrestrial bodies. Eaton and Murata's (1960)

discussion of summit concordancy in the Hawaiian chain supporting the hydrostatic mechanism lead to predictions of the source depth which coincided with the depth of recurrent upper mantle tremors. This hydrostatic mechanism is further validated by the discovery that the Hawaiian Islands are systematically older to the northwest, away from the center of present volcanic activity, indicative of a long-lived source of magma fixed in the mantle beneath the moving lithosphere. The hydrostatic model also predicts that volcano elevation will increase with the thickness of the lithosphere, and Vogt (1974a) found that oceanic volcanoes increase in height as the square root of basement age, supporting the theory that the lithosphere thickens with age as it moves away from mid-ocean ridges.

The hydrostatic mechanism has also been invoked in the study of shields on Mars. Carr (1973) suggested that the height of the largest Tharsis shield Olympus Mons, is hydrostatically limited. Blasius and Cutts (1976) investigated the geophysical implications of the concordant summit heights of the four great Tharsis shields and the correlation of gravity field anomalies with topography in the region. They assumed that the local hydrostatic head on a common magma source limits each shield's height and concluded that the Martian lithosphere thins substantially beneath Tharsis while the crust, if present, is probably thickened.

Ancient low-relief shields which are widely distributed over the surface of Mars may be the closest analogs of the small central volcanic constructs of the Moon and Mercury. Carr (1975a, b) has found a correlation between the age of Martian shields, as determined from impact crater counts, and their relief. This correlation may be a consequence of the gradual thickening of the Martian lithosphere (Carr 1975a, b) allowing younger volcanoes to rise hydrostatically to progressively greater heights. There are other explanations for the low relief of old shields, of course, including isostatic recovery and different physical properties of the lavas. However, in view of the characteristics of the older martian shields, the reliefs and ages of any low shields on the Moon and Mercury are of obvious interest, although comparisons must be approached cautiously because of the expected compositional differences between the terrestrial planets. It seems, moreover, that the hydrostatic hypothesis has some relevance to the Moon; Solomon (1975) has suggested that the low hydrostatic head of magma beneath an early thin lunar lithosphere was responsible for delaying the onset of mare flooding several hundred million years after basin formation. Low relief lunar shields of varying ages may reflect in their summit elevations the gradual thickening of the lunar lithosphere.

Though favorable hydrostatic conditions appear to be necessary for shield volcano formation and for the extrusion of sheet basalts, they may not be a sufficient condition for

these processes to take place. The structural characteristics of the lithosphere also have an important role in the evolution of volcanism. The spacings of volcanoes and associated systems of faults are pertinent to the role of structure in volcano development. The internal spacing of chains of central volcanoes on Earth has been interpreted as reflecting crustal fractures with a spacing approximately equal to the thickness of the lithosphere (Vogt, 1974). An alternative explanation of volcano spacing might be developed from the fluid-dynamic theory of doming of a gravitationally unstable crustal layer (Ramberg, 1967). The regular 1000km spacing of Martian volcanoes has been interpreted to imply an equally thick lithosphere (Vogt, 1974). However, this suggestion is at variance with the photogeological data on the regional tectonics (Blasius and Cutts, 1976).

One significant revelation from this analysis of Viking Orbiter data is that many of the Martian shields have been flooded by flows arising from an external source such that the present relief of the shield does not reflect the original heights of the construct. As a consequence, adjustments to the relief data are needed to interpret the Martian shields in terms of the hydrostatic mechanics.

Of course, lithospheric thickness alone does not completely preordain the tectonic and volcanic evolution of a planet. Solomon and Chaiken (1976) have suggested that some major structural features of terrestrial planets, the largest rifts

and thrusts for example, reflect lithospheric stresses due to bulk thermal evolution and contraction. Major controls on such fundamental trends in thermal evolution are initial accretion temperature, the time of core formation, and internal radioactive heat sources. At one extreme, Martian geologic history has apparently been dominated by extensional tectonics, suggesting gradual build up of internal temperatures, while the most prominent global structures on Mercury are lobate scarps which have been interpreted as thrusts, perhaps reflecting internal cooling. Characteristics of central volcanic constructs, including morphology, may be used to place fundamental constraints on planet evolution. The four great shields of the Tharsis region of Mars have apparently been influenced by prominent planetary scale fault systems, resulting in very assymetric shield growth and influencing the distribution of collapse craters, ridges and rilles on flank surfaces.

REFERENCES- TASK 1

A. Lunar Radar Topography

1. Method

Shapiro, I., Zisk, S.H., Rogers, A.E.E., Slade, M.A.,
and Thompson, T.W., 1972, Lunar Topography: Global
Determination by Radar, Science 178, pp. 939-948.

2. Regional Maps

Zisk, S., 1972, Lunar Topography: First Radar Inter-
ferometer Measurements of the Alphonsus-Ptolemaeus-
Arzachel Region, Science 178, pp. 977-980.

Zisk, S., 1978, Mare Crisium Area Topography: A
Comparison of Earth-Based Radar and Apollo Mapping
Camera Results, in Mare Crisium: The View from
Luna 24, ed. R.B. Merrill and J.J. Papike, pp. 75-80.

Pieters, C.M., Head, J.W., Adams, J.B., McCord, T.B.,
Zisk, S.H., and Whitford-Stark, J.L., 1980,
Late High Titanium Basalts of the Western Maria:
Geology of the Flamsteed Region of Oceanus Procellarus,
J. Geophys. Res. 85, pp. 3913-3938.

B. Comparative Morphometry

Pike, R.J., 1978, Volcanoes on the Inner Planets: Some
Preliminary Comparisons of Gross Topography, Proc.
Lunar Planet. Sci. Conf. 9th, pp. 3239-3973.

Head, J.W., and A. Gifford, Lunar Mare Domes: Classification
and Modes of Origin, Dept. of Geological Sciences,
Brown University, 1978.

REFERENCES - TASK 1 (Cont'd)

C. Blasius, K.R. and J.A. Cutts, Braided Channels Associated with Young Lava Flood Deposits, Tharsis Volcanic Province, Mars, Abstracts of Spring AGU Meeting 1978, p. 310, 1978.

Blasius, K., The smaller central volcanic constructs of the Tharsis region of Mars, Abstracts for the Planetary Geology Field Conf. on the Snake River Plain, Idaho, NASA TM-78436, p. 31, 1977.

Blasius, K.R. and J.A. Cutts, Topography of Martian Central Volcanoes, accepted for publication in Icarus, 1980.

Cutts, J.A. and K.R. Blasius, Rille-Like Valleys of Western Chryse Planitia, Mars: A Lava Erosion Hypothesis for Their Origin, in preparation, 1980.

TASK 2: Origins and Processes of Degradation of
Sub-Kilometer Lunar Craters

2.1 INTRODUCTION

The populations of small craters on lunar maria surfaces have been found to deviate markedly from the ideal equilibrium impact crater population expressed in a cumulative distribution slope of -2 (Boyce 1976; Kuipert et al., 1966; Chapman, 1968). Possible reasons for the deviation from the ideal behavior include the presence of a population of small craters of endogenic origin (Chapman et al., 1970; Fielder et al., 1972; Schultz et al., 1976) differences in energy/diameter scaling realtions in the regolith and bedrock (Fielder et al., 1972; Schultz et al., 1976, 1977); and differential erosion and degradation of craters in the regolith and bedrock (Fielder et al., 1972; Schultz et al., 1976, 1977). It is important to develop a detailed understanding of these effects in order to understand the layered structure of the lunar maria, establish if a population of endogenic craters is distorting crater age determinations, and to examine if relative ages using the crater morphology parameter called D_L are valid.

2.2 BACKGROUND AND PROGRESS REPORT

In the first year's task, we conducted a pilot study of small crater populations in several carefully selected lunar mare regions representative of both red and blue basalt types with both "young" and "old" D_L ages. Craters of diameter

20m to 20km were counted and classified into 40 morphological classes. A description of this compilation and the full data set is given in Appendix 2.1. In our preliminary examination of these data (Appendix 2.2), we reported features incompatible with a simple model of impact cratering and equilibrium degradation and obliteration by the impact process. In particular our "young blue" units show an excess of 100m diameter (largely degraded) craters compared with both the "old red" and "old Blue" provinces studied. The excesses approach factors of 2 to 5 and violate the intuitive expectation that younger units should have fewer craters than older units. Most regions we have measured (mapped in Figure 2.1) share characteristics of small crater populations previously described by Chapman et al and Schultz et al. Figure 2.2 illustrates the total crater populations in five different areas, distinguished by color and D_L age. Figure 2.3 (right) shows the separate distributions for the four morphological classes: 1 to 4 (fresh to degraded), for the "old red" region.

The qualitative differences in distribution of different morphological classes of craters from region to region are discussed in greater detail in our Lunar and Planetary Science Conference abstract (Chapman et al., 1979). We have developed a preliminary interpretation of these data that yields the model size distributions illustrated in Figure 2.3 (left). Major features of this model are: (a) craters are all impact craters with no endogenic population; (b) different diameter

scaling effects due to regolith and basement rock; (c) formation of fresh craters of apparently degraded morphology in certain size ranges comensurate with the scale of the regolith depth; and (d) variations in equilibrium crater densities at different sizes due to differences in efficiency of erosion. Figure 2.3 shows that the model bears at least a qualitative similarity to the actual crater counts for the "old red" region.

If the preliminary interpretation is correct, then there may be no need to hypothesize the existence of large numbers of endogenic craters, as some investigators have supposed (most recently Greeley, Proc. Lun. Plan. Sci. Conf. X, in press). Also there is a greater likelihood that the morphological parameters D_L can be interpreted as a reliable indicator of relative age.

2.3 FUTURE WORK

The Planetary Geology program is funding further work on this project: this includes preparation of the measurements for publication and development of a simple computerized numerical simulation of our phenomenological model for small-crater production and destruction. Through comparisons of data for all regions with the model, it will be possible to establish limits on the degree to which plausible variations in parameters yield the diversity of crater distributions on the lunar maria.

The model will be derivative from models previously devised by Chapman et al., (1970). It will be augmented by

parameters describing the diameter scaling relations in a two-layer model of the lunar surface by the different initial morphology distributions, and be a representation of the differential erosive processes qualitatively described by Schultz et al. Cratering and erosion will proceed through timesteps with appropriate criteria established for the evolution of a crater of a given size through a succession of classes to final obliteration.

In evaluating the results, we will re-examine the local geological context of each region measured to see what other extenuating processes or circumstances might explain any remaining discrepancies with the model. Of course, the regions were originally selected after careful examination of the entire library of lunar imagery at the Tucson Planetary Imaging Data Center to be relatively simple and geologically homogeneous.

The final publication of the data and model will evaluate, as well, the implications of the study for the origin of small craters, the nature of lunar degradation processes, and the implications for the viability of the D_L parameters as a measure of relative age. We will also comment on the implications for genesis of mare basalts of different compositions, to the degree our limited sample of colors and D_L ages permits.

REFERENCES - Task 2

Boyce, J.M. (1976), Proc. Lunar Sci. Conf. 7th, 2717-2728.

Chapman, C.R. (1968), Icarus 8, 1-22.

Chapman, C.R., Aubele, J.C., Roberts, W.J., and Cutts, J.A., (1979), Abstracts of papers submitted to the tenth Lunar and Planetary Science Conference, March 19-23, 1979, 190-191.

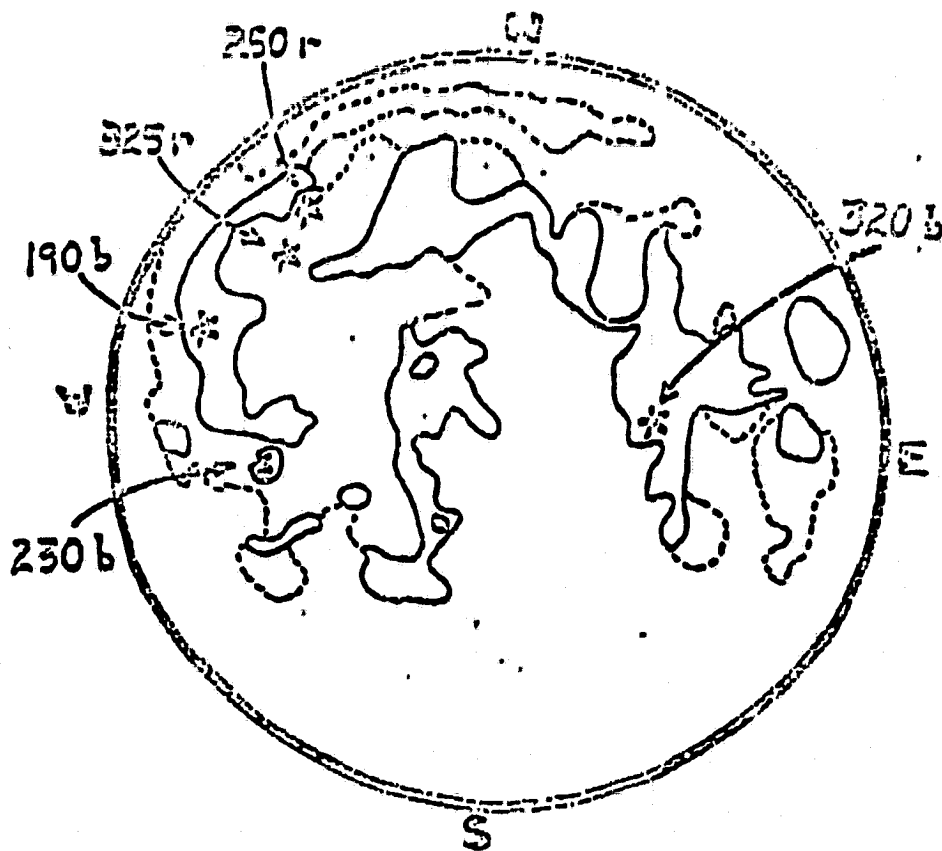
Chapman, C.R., Mosher, J.A., and Simmons, G. (1970), J. Geophys. Res. 75, 1445-1466.

Fielder, G., Fryer, R.J., Titulaer, C., Herring, A.K., and Wise, B. (1972), Phil. Trans. Roy. Soc. London 271, 361-409.

Kuiper, G.P., Strom, R.G., LePoole, R.S., (1966) Ranger 8 and 9, Part 2, JPL Tech. Report 32-800, 35-248.

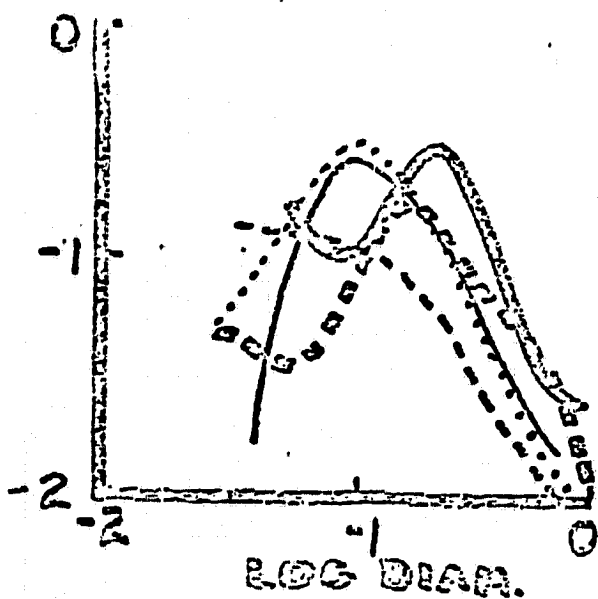
Schultz, P.H., Greeley, R., and Gault, D.E., (1976), Proc. Lunar Sci. Conf. 7th, 985-1003.

Schultz, P.H., Greeley, R., and Gault, D.E., (1977), Proc. Lunar Sci. Conf. 8th, 3539-3564.



Number is D_e age; r = red, b = blue.

FIGURE 2.1



- young blue
- medium-young blue
- .-.- old blue
- medium red
- - - old red

FIGURE 2.2

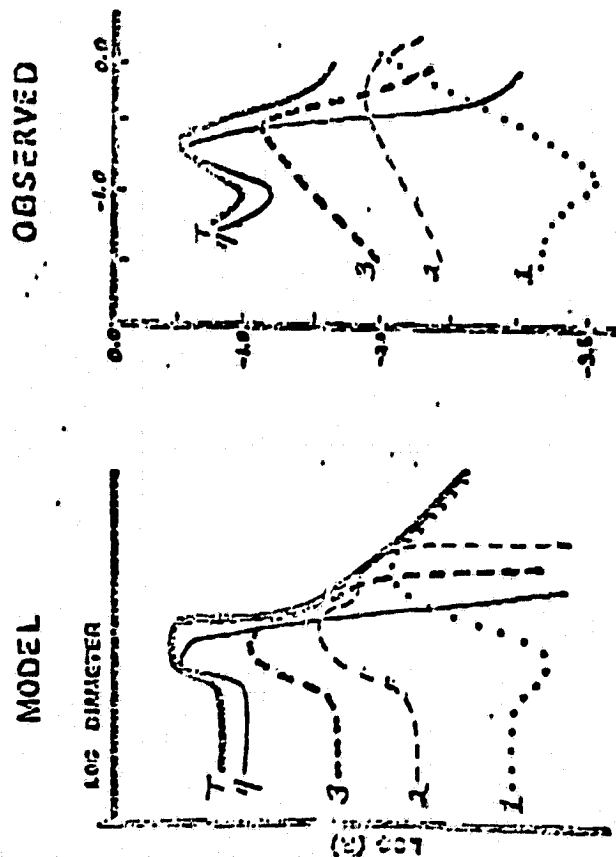


FIGURE 2.3

ORIGINAL PAGE IS
OF POOR QUALITY

APPENDICES

- 1.1 Data Collected on Possible Lunar Volcanic Constructs:
Lunar Domes from Geologic Map.
- 1.2 Topography of Martian Central Volcanoes by Karl R. Blasius and James A. Cutts, Icarus, (in press), 1980.
- 2.1 Data Base Developed in Task 2.
- 2.2 Sub Kilometer Lunar Craters: Origins Ages Processes of Degradation and Implications for Mare Basalt Petrogenesis, C.R. Chapman, J.C. Aubele, W.J. Roberts, and J.A. Cutts, LPSC Abstracts, 1979.

APPENDIX 1.1

**Data Collected on Possible Lunar
Volcanic Constructs: Lunar Domes from
Geologic Maps**

TABLE 1.1: LUNAR DOMES FROM GEOLOGIC MAPS

LAC	Lat.	Lon.	Unit	Background Unit	Isolated?	Mean Diameter (km)	Elevation	(Ref. 1730km) Local Relief (m)
38	52.4°W	28.4°N	CEvd	CEvh	No		5240	Under 200m
38	51.9°W	27.5°N	CEvd	CEvh & CEvs	No		5800	Under 200m
38	54.9°W	27.4°N	CEvd	CEvh & Ipm	No		5200	Under 200m
38	51.4°W	27°N	CEvd	CEvh	No		6175	Under 200m
38	51.8°W	26.7°N	CEvd	CEvh & CEvc	No		6200	Under 200m
38	50.9°W	25.5°N	CEvd	CEvh	No		N O	M A P
38	50°W	20.3°N	Ipd	Ipm			N O	M A P

CEvd - dome material of Valis Schröteri Formation. Forms convex upward domical surfaces; small craters present at summit. Albedo low, same as surroundings.

Ipd - dome material of Procellarum Group. Forms a dome 13km across having a summit crater.

CEvh - Vallis Schröteri Formation. Hummocky member.

CEvs - Vallis Schröteri Formation. Smooth dark member.

CEvc - Vallis Schröteri Formation. Cratered-cone material

Ipm - mare material of Procellarum group.

LAC	Lat.	Lon.	Unit	Background Unit	Isolated?	Mean Diameter (km)	Elevation	(Ref. 1730km) Local Relief (m)
39	50°W	20.3°N	Ipd	Ipm	Yes		N O	M A P
39	36.5°W	28.7°N	Ipd	Ipm	No		5600	Under 200m
39	36°W	28.5°N	Ipd	Ipm & Ipd	No		5500	Under 200m
39	35.5°W	28.5°N	Ipd	Ipm & rc	No		5590	Under 200m
39	32.5°W	19.2°N	Ipd	Ipm	No		N O	M A P

TABLE 1.1 (Cont'd)

(Ref. 1730km)
Local
Relief
(m)

LAC Lat. Lon. Unit Background Unit Isolated? Mean Diameter (km) Elevation

39	30.5°W	19°N	Ipd	Ipm & Iph	No		N O	M A P
39	35.8°W	29.1°N	Ipr	Ipm & If	Yes	15 km	5500	1000

Ipd - dome material of Procellarum Group. Albedo low and uniform. Forms domes up to 55km across and 300m high.

Ipr - rough dome material of Procellarum Group. Albedo low to moderate. Forms rough - topped domes up to 10km across and 600m high above surroundings.

rc - Rille (rima) and chain crater material.

Iph - Hummocky mare material of Procellarum Group.

If - Fra Mauro Formation (ejecta blanket). Exposed in areas of rough topography and on isolated hills.

(Ref. 1730km)
Local
Relief
(m)

LAC Lat. Lon. Unit Background Unit Isolated? Mean Diameter (km) Elevation

41	10°E	30.9°N	Ipd	Ipm	Yes		N O	M A P
41	.6°W	27.8°N	Ipd	Ipm & Cc	Yes		5200	Under 200m
41	1.4°E	26.1°N	Ipd	Ipm & Cc	Yes	4.5 km	5315	Under 200m
41	4.5°W	22°N	Ipd	Ipm & Esc	No	1 km	5683	Under 200m
41	4.1°W	21.4°N	Ipd?	Ipm	No		5400	Under 200m
41	4.5°W	20.7°N	Ipd	Ipm	No		5300	Under 200m
41	8.8°W	18°N	Ipd	Ipm, Esc, Csc3	No		N O	M A P
41	6.5°W	18.5°N	Ipd	Ipm, Ifhl, Cs, Ec	No		N O	M A P

Cc - Crater material, undifferentiated. Small craters with bright haloes.

Esc - Satellite craters. Shallow craters with low rounded rims and irregular indistinct outlines.

Csc3 - Satellite craters. Commonly elongated.

TABLE 1.1 (Cont'd)

LAC 41 (cont'd.)Ifhl - Fra Mauro Formation. Generally moderate albedo.Cs - Slope material. Occurs on or at base of deep slopes.Ec - Crater material, undifferentiated. Craters too small to permit identification.

LAC	Lat.	Lon.	Unit	Background Unit	Isolated?	Mean Diameter (km)	Elevation	(Ref. 1730km) Local Relief (m)
42	10°E	30.9°N	Ip _d	Ifh & Ip _m 4	yes		N O M A P	

Ifh - Fra Mauro Formation; hummocky facies.Ip_m - Mare material. Albedo: .060 - .061.

LAC	Lat.	Lon.	Unit	Background Unit	Isolated?	Mean Diameter (km)	Elevation	(Ref. 1730km) Local Relief (m)
43	32.1°E	22.6°N	Ip _{Ld}	Ip _h & Ip	Yes	10km	7300	800
43	35.5°E	20.3°N	Ip _{Ld}	Ip, Im, & Ip _h	Yes	15.5km	5900	1000
43	36.5°E	17.7°N	Ip _{Ld}	Ip _h , Ip & Im2	Yes		N O M A P	
43	44.8°E	25.2°N	Ip _{Ld}	It	No		N O M A P	
43	42.4°E	26.2°N	Ip _{Ld}	It, Ip, Ip _h , Ip _{Ir}	No		N O M A P	
43	43.1°E	27.3°N	Ip _{Ld}	Ip, Ip _{Ir} , Ip _h	No		N O M A P	
43	48.1°E	28.9°N	Ip _{Ld}	Ip, It, Ip _h	Yes		N O M A P	

Ip_{Ld} - dome material, smooth and massive to hummocky and bulbous. Irregular to nearly circular outlines.Ip_h - material of round smooth hills and hummocks.Ip - plains material; resembles older mare material but is brighter and more highly pitted with small craters.

TABLE 1.1 (Cont'd)

LAC 43 (cont'd.)

- It - Terra material. Smooth, gently undulating to low hilly terrain.
 IpIr - Material of rugged terra. Ranges from smooth material having moderate relief to large hills and mountains having high relief.
 Im - Mare material.

LAC	Lat.	Lon.	Unit	Background Unit	Isolated?	Mean Diameter (km)	Elevation	(Ref. 1730km) Local Relief (m)
44	60.0°E	19.3°N	EId	Im	(1 of pair) Yes	N O	M A P	
44	62.1°E	18.4°N	EId	Im	(1 of pair) Yes	N O	M A P	
EId - Material of cratered domes. Small, irregular depression at summit.								

LAC	Lat.	Lon.	Unit	Background Unit	Isolated?	Mean Diameter (km)	Elevation	(Ref. 1730km) Local Relief (m)
59	9.5°W	9.35°N	IpD	IpM	(1 of pair) Yes?			
59	9.6°W	9.4°N	IpD	IpM	(other 1 of pair) Yes?			
59	0.1°W	4.1°N	IpD	Ica & Icah?	Yes			
59	9.4°E	8.3°N	IpD	Ipml & Ifs	Yes			
59	4.5°E	8.8°N	IpD?	Ica	Yes			
59	6.3°E	13.6°N	IpD	Ipml & IpM2	No			

TABLE 1.1 (Cont'd)

(Ref. 1730km)

LAC	Lat.	Lon.	Unit	Background Unit	Isolated?	Mean Diameter (km)	Elevation	Local Relief (m)
59	6.1°E	13.6°N	Ipd?	Ipm1 & Ipm2	No			
59	6.05°E	13.8°N	Ipd?	Ipm1	No			
59	4.9°E	13.5°N	Ipd?	Ipm2	No			
59	5.7°E	15.2°N	Ipd	Ipm1 & Ipm2	No			
59	6.75°E	14.6°N	Ipd	Ipm2	No			
59	7.4°E	15.1°N	Ipd	Ipm2	No			
59	7.2°W	2.9°N	Eisd	Ips & Ipm1	No			
59	7.1°W	4°N	Eisd	Eis	No			
59	8.1°E	9.2°N	Eisd?	Eis & Icah	No			
59	7.7°E	9.5°N	Eisd	Eis & Ips	No			
59	6.8°E	10.3°N	Eisd	Eis	No			
59	6.8°E	10.8°N	Eisd	Eis & Ipm2	No			
59	6.7°E	11.3°N	Eisd	Eis	No			
59	6°E	12.4°N	Eisd	Ipm2	No			
59	6.4°E	12.2°N	Eisd	Ipm2 & Eis	No			
59	6.7°E	12.4°N	Eisd	Ipm2	No			
59	7°E	12.2°N	Eisd	Ipm2, Eis, Ifh	No			
59	8.8°W	6.8°N	Eisd	Ipm & Eis	No			
59	9.2°W	7.8°N	Eisd	Ipm & Eis	No			
59	8.9°W	7.7°N	Eisd	Eis	No			
59	8.3°W	7.9°N	Eisd	Ipm & Eis	No			
59	7°W	8.2°N	Eisd	Ipm	No			
59	8.4°W	8°N	Eisd	Ipm & Eis	No			
59	8.2°W	8.2°N	Eisd	Ipm & Eis	No			

ORIGINAL PAGE IS
OF POOR QUALITY

TABLE 1.1 (Cont'd)

LAC	Lat.	Lon.	Unit	Background Unit	Isolated?	Mean Diameter (km)	Elevation	Local Relief (m)
59	8.3°W	8.5°N	EIsd	Ipm	No			
59	7.6°W	8.1°N	EIsd	Ipm	No			
59	7.9°W	8.5°N	EIsd	Ipm & EIs	No			
59	7.8°W	8.9°N	EIsd	Ipm & EIs	No			
<p><u>Ipd</u> - dome material of Procellarum Group. Form circular or elliptical domes broad in proportion to height. Flanks convex in profile, some domes flattened on top. Some have summit craters. Albedo & surface texture similar to Ipm units.</p> <p><u>EIsd</u> - dome material of Sulpicius Gallus Formation. Occurs as elliptical to elongate domes, steeper than mare domes; smooth.</p>								
								(Ref. 1730km)
60	24.1°E	11.4°N	Ipd	Ipm2	Yes		N O M A P	
60	20.7°E	9.4°N	Ipd	Ipm2	No		N O M A P	
60	20.9°E	9°N	Ipd	Ipm2	No		N O M A P	
60	21.2°E	8.6°N	Ipd	Ipm2	No		N O M A P	
60	21.6°E	7.7°N	Ipd	Ipm2	No		N O M A P	
60	19.9°E	6.3°N	Ipd	Ipm2	No		N O M A P	
60	22°E	5.4°N	Ipd	Ipm2	No		N O M A P	
60	29.7°E	13.1°N	Ld	Ipm2	Yes	4 km	6200	500
60	20.7°E	14.8°N	Ld	Ifs & Ipm4	Yes	13 km	6300	1200
60	16.9°E	13.9°N	Ld	Ipm2 & Ipm4	No	6 km	6900	900
60	15.9°E	12.8°N	Ld	Ifs & Ipm4	No		7500	Under 200m
60	15.7°E	12.7°N	Ld	Ifs & Ipm4	No	4 km	7300	300

TABLE 1.1 (Cont'd)

LAC	Lat.	Lon.	Unit	Background Unit	Isolated?	Mean Diameter (km)	Elevation	Local Relief (m)
						5 km	7400	900
60	15°E	12.2°N	Ld	Ifs & Ipm2	No		7400	600
60	14.6°E	12°N	Ld	Ifs & Ipm2	No	4.75 km		
60	14.4°E	11.9°N	Ld	Ifs	No			
60	14.7°E	11.6°N	Ld	Ifs, Ipm2, Ipm4	No		N O	M A P
60	14.9°E	12.8°N	Ld	Ifh & Ipm2	No		7400	Under 200m
60	13.4°E	11.8°N	Ld	Ifh & Ipm4	No		N O	M A P
60	13.7°E	11.4°N	Ld	Ipm4 & Ifh	No		N O	M A P
60	12.9°E	11.3°N	Ld	Ifs & Ipm4	No		N O	M A P
60	13.9°E	10.9°N	Ld	Ifh & Ipm4	No		N O	M A P
60	10.7°E	9.2°N	Ld	Ifh & Eib	No		N O	M A P
60	11.4°E	9.2°N	Ld	Imp4 & Eib	No		N O	M A P
60	12.4°E	5.8°N	Ld	Eib?	No		N O	M A P
60	14.1°E	6.2°N	Ld	Ifh?	No		N O	M A P
60	14.1°E	6.5°N	Ld	Ifh? & Ifs	No		N O	M A P
60	15.7°E	6.6°N	Ld	Ifs, Ica, dd	No		N O	M A P
60	16°E	6.9°N	Ld	Ifs	No		N O	M A P
60	16.3°E	6.5°N	Ld	Ifs & Ica	No		N O	M A P
60	16.1°E	6°N	Ld	Ifs, Ifh?, Ica	No		N O	M A P
60	12.9°E	8.7°N	dd	Eib, Ica?, Ifs	Yes		N O	M A P
60	16°E	6.5°N	dd	Ifs, Ld, Ica	No		N O	M A P
60	16.7°E	7.5°N	dd	Ifs	No		N O	M A P

Ld - Terra dome material; light domes. Outline round, elliptical or irregular. Rougher and steeper than mare domes. Albedo high to very high; some domes extremely bright in all i-luminations.

TABLE 1.1 (Cont'd)

LAC 60 (cont'd.)

- dd - Terra dome material; dark domes. Convex profile, broader and lower than light domes, appear to be composed of several lobes. Albedo intermediate.
- Ipm - Procellarum Group; volcanic materials: flows or ash beds or both.
- Els - Topographically mainly hummocky. Sulpicius Gallus Formation.
- Icah - Hilly member of Cayley Formation.
- Ifs - Smooth member. Fra Mauro Formation.
- Ifh - Hummocky member. Fra Mauro Formation.
- Elb - Rough hummocky surface. Boscovich Formation.
- Ica - Surface generally flat and smooth. Cayley Formation.

LAC	Lat.	Lon.	Unit	Background Unit	Isolated?	Mean Diameter (km)	N O	Elevation	(Ref. 1730km) Local Relief (m)
61	44.7°E	9.8°N	It d	Its, pIc, pIth	Yes				
61	44.8°E	13.8°N	It d	Ip, pIci, pIth	Yes	8 km		6200	1100
61	41.5°E	14°N	It d	Iph & Its	Yes	8 km		6600	1000
61	49.8°E	15.1°N	EIm d	Im 3	Yes	2 km		3700	200
61	36.1°E	15.6°N	EIm d?	Im 2	No			6300	Under 200m
61	35.6°E	15.6°N	EIm d?	Im 2	No			6300	Under 200m
61	35.5°E	15.8°N	EIm d?	Im 2 & EId e	No			6400	Under 200m
61	35.2°E	15.5°N	EIm d?	Im 2, Im 1, Its	No			6500	Under 200m
61	34.8°E	15°N	EIm d	Im 1 & Its	No			6400	Under 200m
61	35°E	14.7°N	EIm d	Im 1	No			6300	Under 200m

TABLE 1.1 (Cont'd)

LAC	Lat.	Lon.	Unit	Background Unit	Isolated?	Mean Diameter (km)	Elevation	(Ref. 1730km)	
								Local Relief (m)	
61	34.7°E	14.4°N	EImd	Im1	No		6200	Under 200m	
61	34.2°E	14.2°N	EImd	Im1	No		6150	Under 200m	
61	33°E	15.1°N	EImd	Im1 & Im2	No		6400	Under 200m	
61	32°E	15.7°N	EImd	Im2, Im3, p1c	No		6300	Under 200m	
61	31.3°E	15°N	EImd	Im3	No		6300	Under 200m	
61	35.7°E	14.3°N	EImd	Im3	No		6400	Under 200m	
61	35.6°E	14.1°N	EImd	Im3	No		6400	Under 200m	
61	35.9°E	14.3°N	EImd	Im2 & Im3	No		6400	Under 200m	
61	36.4°E	13.8°N	EImd	Im2	No		6400	Under 200m	
61	36.3°E	13.4°N	EImd	Im2	No		6400	Under 200m	
61	36.9°E	13.7°N	EImd	Im2	No		6400	Under 200m	
61	31.1°E	13.2°N	EImd	Im2 & Im3	No	9 km	6000	600	
61	32.4°E	12.5°N	EImd	Im3	No		6200	Under 200m	
61	30.1°E	12.2°N	EImd	Im2	No		6300	Under 200m	
61	30.2°E	12.1°N	EImd	Im2	No		6300	Under 200m	
61	30.2°E	11.2°N	EImd	Im3	No		N O	M A P	
61	31.9°E	10.7°N	EImd	Im3	No		N O	M A P	
61	32.4°E	10.7°N	EImd	Im3	No		N O	M A P	
61	32.3°E	10.9°N	EImd	Im3	No		N O	M A P	
61	34°E	10.8°N	EImd	Im3	No		N O	M A P	
61	35.1°E	10.1°N	EImd	Im2	No		6700	Under 200m	
61	37.1°E	8.7°N	EImd	Im3	No		6650	Under 200m	
61	37.7°E	8.4°N	EImd	Im3	No		6600	Under 200m	
61	36.8°E	7.5°N	EImd	Im3	No		N O	M A P	

TABLE 1.1 (Cont'd)

(Ref. 1730km)

LAC	Lat.	Lon.	Unit	Background Unit	Isolated?	Mean Diameter (km)	Elevation	Local Relief (m)
61	37.6°E	7.2°N	EImd	Im3	No		N O M A P	
61	38.4°E	7.3°N	EImd	Im3	No		N O M A P	
61	33.9°E	2.4°N	EImd	Ctm & Em	Yes		6500	Under 200m
61	30.8°E	14.3°N	Eild	Im3	No	8 km	6400	300
61	32.4°E	14.5°N	Eild	Im2 & Im3	No		6100	Under 200m
61	32.2°E	14.3°N	Eild	Im2	No		6000	Under 200m
61	32.4°E	13.8°N	Eild	Im2 & Im3	No		6000	Under 200m
61	32.6°E	13.7°N	Eild	Im2 & Im3	No		6000	Under 200m
61	36.2°E	14°N	Eild	Im2 & Im3	No		6400	Under 200m
61	36.5°E	13.7°N	Eild	Im2	No		6400	Under 200m
61	30.3°E	11.6°N	Eild	Im2 & Im3	No		N O M A P	
61	32.3°E	12°N	Eild	Im3	No		6200	Under 200m
61	33.2°E	13.8°N	Eild	Im3	No		6000	Under 200m
61	33.1°E	10.5°N	Eild	Im3	No		N O M A P	
61	35.4°E	14.9°N	Eidd	Im1, Im2, Im3	No		6300	Under 200m
61	35.6°E	14.8°N	Eidd	Im2 & Im3	No		6300	Under 200m
61	35.7°E	14.6°N	Eidd	Im2 & Im3	No	2 km	6400	200
61	31.6°E	10.2°N	Eird	Im3	Yes		N O M A P	
61	36.7°E	7.4°N	Eird	EImd	(1 of pair)		N O M A P	
61	36.8°E	7.5°N	Eird	EImd & Im3	(1 of pair)		N O M A P	
61	38.2°E	15.9°N	EImd	Im2	Yes	3.5 km	6400	100

Itld - Terra dome material. Smooth to somewhat rough. Steeper than mare domes; irregular but generally circular. Same diameter range as mare domes.

TABLE 1.1 (Cont'd)

LAC 61 (cont'd.)

EImd - Typical mare dome material. Smooth low domes with gentle convex upward profile. Circular or elliptical.

EILD - Light dome material. Similar to typical domes but higher relative to width and brighter.

EIdd - Dark dome material. Steeper, darker and more elongate.

EIRD - Rough dome material. Rough surface with tiny craters or rough ridge superimposed on other dome.

Im1, Im2, Im3 - Flat or undulatory terrain. Mare materials.

Ctm - Terra mantling material. Forms undulatory terrain masking underlying small unmapped craters.

Em - Mare material. Forms flat, dark surfaces.

Its - Smooth terra material. Forms smooth-surfaced gentle hills or undulatory terrain.

PIC - Crater material. Circular outline, commonly interrupted.

pIci - Irregular crater materials. Irregular outline with marked re-entrants.

pIth - Hilly terra material. Forms moderately elevated terrain with variable nondistinctive surface texture subdued to pocked or bumpy.

Ihp - Hilly and pitted material. Hilly terrain with numerous irregular rimless or rimmed pits.

LAC	Lat.	Lon.	Unit	Background Unit	Isolated?	Mean Diameter (km)	(Ref. 1730km)	
							Elevation	Local Relief (m)
62	52.6°E	1.6°N	EImd	EIm	No		4950	Under 200m
62	52.6°E	1.3°N	EImd	EIm	No	2.5 km	4950	100
62	55.6°E	1°N	EImd	EIm	No	7.5 km	5000	400
62	55.7°E	.4°N	EImd	EIm	No		4900	Under 200m

TABLE 1.1 (Cont'd)

LAC 62 (cont'd.)

EImd - Mare dome material. Broad, low; tops flat or rough.EIm - Mare or mantling material. Darkest and least cratered unit in area.

LAC	Lat.	Lon.	Unit	Background Unit	Isolated?	Mean Diameter (km)	Elevation	(Ref. 1730km) Local Relief (m)
75	34.8°W	7.6°S	Pd	Pm	Yes		N O M A P	
75	30°W	3.9°S	Pd	Pm	Yes		N O M A P	

Pd - Dome material. Reflectivity low and local contrast in reflectivity small.Pm - Mare material. Reflectivity low with small local contrast.

LAC	Lat.	Lon.	Unit	Background Unit	Isolated?	Mean Diameter (km)	Elevation	(Ref. 1730km) Local Relief (m)
76	30°W	3.9°S	Ipd	Ipm	Yes		N O M A P	
76	24.3°W	3.4°S	Ipd	Ipm, Ecr, If	Yes		N O M A P	
76	29.3°W	12.5°S	Ipd?	Ipm & Ccr	No		N O M A P	
76	27.3°W	12.7°S	Ipd?	Ipm	No		N O M A P	
76	26.9°W	14.2°S	Ipd	Ipm	No		N O M A P	
76	19.8°W	11.8°S	Ipd	Ipm	Yes		5600	Under 200m

TABLE 1.1 (Cont'd)

LAC 76 (cont'd.)

- Ecr - Crater rim material (ejecta blanket).
Ccr - Crater rim material (ejecta blanket).
If - Fra Mauro Formation. Ejecta blanket. Topography characterized by numerous hills and depressions.

79	49°E	2.5°S	Imd	Im	No	5300	Under 200m
79	49.7°E	1.7°S	Imd	Im	No	5400	Under 200m

- Imd - Material of smooth dome-like features in maria.
Im - Mare material. Fairly smooth, level.

<u>MISSING MAPS</u>		<u>MAPS WITH NO DOME MATERIAL</u>	
LAC 63	LAC 84	LAC 40	
LAC 64	LAC 85	LAC 78	
LAC 65	LAC 86	LAC 80	
LAC 66	LAC 100		
LAC 77	LAC 101		
LAC 81	LAC 102		
LAC 82	LAC 103		
LAC 83	LAC 104		

NOTE: LAC 77 is on the near side of the Moon. The rest are on the far side.

LAC 77

LAT	LON	UNIT	BACKGROUND UNIT	ISOLATED?	ELEVATION	LOCAL RELIEF (REF. 1730 km)
1.2°S	8.2°E	d	Ica	YES	N O M A P	
5.5°S	7.6°E	d	Ica & It	NO	>200m	8200
4°S	4.8°E	d	Ica	NO	>200m	7500
5.4°S	.2°W	d?	pIU & It	NO	>200m	7500
5.7°S	1°E	d	pIu & It	NO	>200m	8700
6.5°S	.8°W	d	EIcr	NO	>200m	8000
4.6°S from 3.9°E		d	Ica with	large cluster of very small domes	>200m	7600
6.5°S to 6.6°E		d	one touching It		>200m	7100

d - Domical or conical hill having summit crater

pIc - Rim and wall of crater

pIu - Undivided material. Rugged uplands, extensively faulted.

Ica - Cayley Formation. Forms level or nearly level plains in terra.

It - Terra material. A mantling material in hilly uplands.

EIcr - Crater rim. Arzachel rim material (?); gently hummocky to rolling.

DIFFERENCES BETWEEN LAC CHARTS
AND LARGE MAP OF NEAR SIDE OF MOON

<u>LAC</u>	<u>NOTES</u>
38	Cluster of CEvd missing from big map. <u>CEvd</u> - dome material of Vallis Schröteri Formation.
39	CED shown on big map missing from LAC 39. <u>Ced</u> - dome material.
43	Clusters of IpId missing from big map. <u>IpId</u> - smooth and massive to hummocky and bulbous domes.
44	All dome material (EId) from LAC 44 missing from big map but they are very small. <u>EId</u> - material of cratered domes.
61	Part of cluster of EId missing from big map along with omission of Itd from big map. <u>EId</u> - light mare dome material. <u>Itd</u> - terra dome material.
62	All dome material (EImd) from LAC 62 missing from big map.
76	All dome material (IpId), except for one large half dome shared by LAC 75, missing from big map.
79	All dome material (Imd) from LAC 79 missing from big map. <u>Imd</u> - material of smooth domes in maria.
77	All dome material (d) from LAC 77 missing from big map. <u>d</u> - domical or conical hill having summit crater.

TABLE 1.2:

LUNAR MARE DOMES
(from Head and Gifford, 1978)

Name	Class	Coordinates		Diameter km.	Shape		Summit Pit	Imagery	Reliability
		Lat.	Long.						
Cauchy 1	I	7.7°N	38.5°E	10	C		X	CLAD7, D3.	A
Cauchy 2	III	7.8°N	36.7°E	9.5	C		X	D3, D7	A
Cauchy 3	III	8.5°N	37.7°E	6	C		X	AS8-13-2344	B
Cauchy 4	III	8.7°N	37.1°E	5.5	C		X	AS8-13-2344	B
Cauchy 5	III	7.2°N	37.6°E	5	C		X	AS8-13-2344	A
Sinas 1	I	10.6°N	32.9°E	10.5	E		X	D8 AS17-23604	A
Sinas 2	VI	10.7°N	32.9°E	6.5	E		X	D8	B
Sinas 3	III	11.0°N	32.2°E	8	C		X	D8	A LHC 61
Jansen 1	VI	11.8°N	31.4°E	5.7	E		-	D8	B
Jansen 2	VI	11.2°N	30.2°E	4.5	C		-	D8	B LHC 61
Jansen 3	VI	11.7°N	30.9°E	4	C		-	D8	B
Jansen 4	VI	11.9°N	31.3°E	5.5	C		-	D8	B
Jansen 5	III	12.5°N	32.4°E	6	E		-	D8	B LHC 61
Jansen 6	I	11.9°N	32.3°E	16x12.5	I		2.8	D8	A LHC 61
Jansen 7	III	11.8°N	33.1°E	11x4.7	E		4.8x1.4	D8	A
Jansen 8	III	10.7°N	33.9°E	4.5	E		X	D8	B
Arago 1	VII	6.2°N	19.9°E	18	I		-	D11	A
Arago 2	VII	7.6°N	21.5°E	13 x 21	E		X	D11	A LHC 60
Arago 3	III	8.5°N	21.2°E	7	C		-	D11	B
Arago 4	III	9.0°N	20.9°E	8	C		-	D11	B

TABLE 1.2 (Cont'd)

Name	Class	Coordinates		Diameter km.	Shape	Summit		Imagery	Reliability
		Lat.	Long.			Pit			
Arago 5	III	9.3°N	20.7°E	8	C	-		D11	B
Arago 6	VI	11.3°N	24.1°E	5	C	-		D11	B
Manilus 1	I	15.3°N	5.6°E	12.5	C	X		D10	A
Manilus 2	VI	15.1°N	7.6°E	4.5	C	-		D10	C
Manilus 3	III	15°N	7.4°E	6.5	C	X		D10, D13	B
Manilus 4	VI	14.6°N	6.7°E	5.5	C	-		D10, D13	A
Manilus 5	III	13.5°N	6.7°E	19.3x8	I	X		D10	B
Manilus 6	VI	13.6°N	6.1°E	4.5	C	-		D10	B
Manilus 7 Grp of 3	VI	13.5°N	6.1°E	~2 each	E	-		D10	B
Mashelyne 1	I	2.7°N	33.5°E	6x8	E	X		D7	A
Triesnecker 1	V	2.6°N	0.4°E	10.7	I	-		D12	C
M. Serenitatis 1 (Linne ALPHA)	II	30.8°N	10.2°E	29	C	-		C11	A
Hortensius 1	II	7.1°N	28.4°W	7.9	C	2.6		CLA D23	A
Hortensius 2	I	7.1°N	28.0°W	5.6	C	1.5		CLA D23	A
Hortensius 3	II	7.6°N	27.8°W	8.0	E	Left 1.7x2.4 Right 1.5		CLA D23	A
Hortensius 4 (Hortensius SIGMA)	I	7.6°N	27.5°W	6.8	C	1.5		CLA D23	A
Hortensius 5	I	7.9°N	27.6°W	6.8	E	1.5		CLA D23	A
Hortensius 6	II	7.9°N	27.3°W	7.0	E	-		CLA D23	B
Hortensius 7	V	9.0°N	29°W	~1	I	-		CLA D20	C
Hortensius 8 Grp of 2	VI	7.8°N	27°W	~3	I	-		D19, D20	C

3 LHC 60

A LHC 42

TABLE 1.2 (Cont'd)

Name	Class	Coordinates		Diameter km.	Shape		Summit Pit	Imagery	Reliability
		Lat.	Long.						
Hortensius 9 Grp of 4	VI	5.5°N	28°W	~4	I	-	-	D19	C
Tobias Mayer 1	II	12.9°N	31.3°W	13	C	X	-	D22, D23	B
T. Mayer 2	II	13.1°N	31.1°W	13	C	3.6x1.4	-	D23	B LHC. 60
T. Mayer 3	II	13.6°N	30.5°W	13	C	2.7x1.4	-	D23, AS17-23740	B
T. Mayer 4	II	12.7°N	30.1°W	16	C	1.2	-	D23	B
T. Mayer 5	III	12.3°N	29.4°W	10.5	I	X	-	D23	C
T. Mayer 6	II	12.0°N	27.4°W	10	C	X	-	D23	C
T. Mayer 7	V	14°N	31.4°W	10	I	-	-	D20	C
Milichius 1	I	10.1°N	31.2°W	9	C	X	-	CLA D22	A
Milichius 2	IV	10.5°N	31.5°W	8	I	-	-	D25	D
Milichius 3	II	10.4°N	32°W	10.5	I	X	-	D22, D25	B
Milichius 4	V	10.9°N	32.6°W	13	I	X	-	D22	A
Milichius 5	VI	8.4°N	32.6°W	6.5	E	-	-	D25	C
Eratosthenes 1	IV	18°N	8.5°W	19x28	I	-	-	D14	C
Eratosthenes 2	V	18.7°N	7.2°W	19	I	-	-	D16, C12	B
Eratosthenes 3	V	21°N	4.6°W	8	C	-	-	C9, C12, AS17-153-23587	B
Eratosthenes 4	V	22.3°N	4.6°W	15	C	-	-	C9, C12, AS17-153-23587	B
Euler 1	V	18.9°N	30.5°W	15	E	-	-	C15, C16	B
Reinhold 1 (Reinhold DELTA)	III	2°N	25.5°W	8	C	-	-	D19, D20	B
Gambart 1	II	2.8°N	12.4°W	13.5	C	X	-	D15	B
Gambart 2	V	2.5°N	12.6°W	5	I	-	-	D15	C

TABLE 1.2 (Cont'd)

Name	Class	Coordinates Lat. Long.	Diameter km	Shape	Summit Pit	Imagery	Reliability
Aristarchus 1 (Herodotus OMEGA)	III	20.3°N 50°W	11	E	X	C21, C22, AS15-88-11980	A
Vitruvius 1	I	14.4°N 35.6°E	8.5	C	1.5	D8	A } LHC 61
Vitruvius 2	III	14.6°N 35.2°E	6.5	I	1.5	D8	B }
Vitruvius 3	III	14.9°N 34.9°E	10.5	C	-	D8	A }
Vitruvius 4	VI	14.5°N 34.6°E	5	C	-	D8	A } LHC 61
Vitruvius 5	I	14.3°N 33.9°E	8.7	C	2	D8	A
Vitruvius 6	VI	14.2°N 33.2°E	6	C	-	D8	A
Vitruvius 7	VI	14.8°N 32.2°E	7	C	-	D8	A
Vitruvius 8	VI	15.0°N 32.5°E	6.5	C	-	D8	A
Vitruvius 9	VI	14.2°N 32.2°E	5.0	C	-	D8	A
Vitruvius 10	III	14.6°N 32.6°E	9.5	C	-	D8	A
Vitruvius 11	II	15.8°N 35.5°E	6.0	I	X	AS17-M-306	A LHC 61
Vitruvius 12	III	15.2°N 37.7°E	5.0	E	-	AS17-M-305	B
Vitruvius 13	V	13.6°N 39.4°E	12.0	I	X	AS17-M-306	A
Kies 1	I	26.7°S 24.4°W	11	C	X	F20 (CLA)	A
Rumker 1	II	40.5°N 58.2°W	9	C	-	LO IV 163 H2	A
Rumker 2	III	42.0°N 57.8°W	3.5	I	1.0	LO IV 163 H2	A
Orientalis 1	II	18.0°S 85.0°W	8	I	1.5	LO IV 187 H2	A
Wollaston 1	II	30.2°N 48.0°W	6	C	-	LO IV 151 H3 AS15-88-11979 AS15-M3-2199	A LHC 43

ORIGINAL PAGE IS
OF POOR QUALITY

APPENDIX 1.2

TOPOGRAPHY OF MARTIAN
CENTRAL VOLCANOES

Karl R. Blasius

James A. Cutts

Planetary Science Institute
Science Applications, Inc.
283 So. Lake Avenue, Ste. 218
Pasadena, Calif. 91101

Accepted for publication by ICARUS

November 1980

PSI Contribution #136

36 Pages
7 figures
3 tables
Appendix:
4 pages
2 figures

Running Head:

MARTIAN VOLCANO TOPOGRAPHY

Direct proofs to:

Karl R. Blasius
Planetary Science Institute
283 S. Lake Street, Suite 218
Pasadena, CA 91101

ABSTRACT

New topographic maps of six large central volcanoes on Mars are presented and discussed. These features are Olympus Mons, Elysium Mons, Albor Tholus, Ceraunius Tholus, Uranus Tholus, and Uranus Patera. Olympus Mons has the general form of a terrestrial basaltic shield constructed almost entirely from lava flows; but with 20 to 23 km of relief it is far larger. Flank slopes average about 4° . A nominal density calculated from the shield volume and the local free air gravity anomaly is so high that anomalously dense lithosphere probably underlies the shield. Uranus Patera is a similar feature of much lower present relief, about 2 km, but its lower flanks have been buried by later lava flood deposits. Elysium Mons has about 13 km of local relief and average slopes of 4.4° , not significantly steeper than those of Olympus Mons. Its upper flank slopes are significantly steeper than those of Olympus Mons. We suggest Elysium Mons is a shield volcano modified and steepened by a terminal phase of mixed volcanic activity. Alternatively, the volcano may be a composite cone. Albor Tholus is a partially buried 3 km-tall shield-like construct. Ceraunius and Uranus Tholus are steeper cone-like features with relief of about 6 and 2 km, respectively. Slopes are within the normal range for terrestrial basaltic shields, however, and topographic and morphologic data indicate burial of lower flanks by plains forming lavas. These cones may be lava

shield constructs modified by a terminal stage of explosive activity which created striking radial patterns of flank channels. Differences among these six volcanoes in flank slopes and surface morphology may be primarily consequences of different terminal phases of volcanic activity, which added little to the volume of any construct, and burial of shallow lower flanks by later geologic events. Additional topographic data for Olympus Mons, Arsia Mons, and Hadriaca Patera are described. The digital techniques used to extract topographic data from Viking Orbiter stereo images are described.

INTRODUCTION

Among the large surface features of Mars which evidence internal activity, the great central volcanoes are particularly dear to planetary geologists, for they are easily recognized features with seemingly well understood terrestrial analogues. Peculiar terrains in apparent source regions of some channels, vast canyon or trough systems, and the broad uplands with large free air gravity anomalies are all far more difficult to interpret from a terrestrial perspective. During the Viking Extended Mission in 1978 an opportunity arose to acquire a systematic stereo imaging data set which could be used to characterize great volcanoes and other large-scale features over most of the surface of Mars. That opportunity was fully exploited, and this paper reports the first photogrammetric analyses of those data, three topographic maps showing six great central volcanoes. Other volcano topographic data derived from stereo imaging acquired earlier in the Viking Mission is also described.

DATA

The Viking High Altitude Systematic Stereo Imaging (HASSI) data are a set of about 1,000 images that were acquired by Viking Orbiter 1 from ranges of 20,000 to 34,000 km during the period February to November 1978 (Orbits 601 to 854). This data set contains overlapping stereo imaging for most of the

surface of Mars (20°S to 90°N latitude) at resolutions ranging from 500 to 850 meters per picture element (pixel) under similar lighting conditions of early to mid-morning local time. An index listing all Viking Orbiter images, including these, by location is available from the National Space Science Data Center (NSSDC)* (Document ID75-075A01I).

Other stereo imaging at higher resolution was acquired by the Viking Orbiters. These data are listed in the above document, but stereo pairs are not explicitly identified within the greater volume of non-stereo data. To ease this problem for the student of Mars, a catalog and user's guide to better quality stereo data has been prepared and is now in press (Blasius et al., 1980).

In addition to the images themselves, topographic mapping required engineering support data describing camera location and orientation. The data used to obtain the results reported here are from the Supplementary Experiment Data Record (SEDR) (NSSDC Documents 75-075A-01E and 75-083A-01G). These data, of course, have associated uncertainties which lead to random and systematic errors in compiled topographic maps. In general, these errors are similar in magnitude and character to those found from evaluation of Mariner 9 stereo images of Mars (Blasius, 1973 and Wu et al., 1973). Unless one attempts to measure

*or World Data Center A, NASA, Goddard Space Flight Center, Greenbelt, Maryland 20771

parrallax differences smaller than a pixel, the principal problem encountered in compiling a topographic map is the absence or limited accuracy of geodetic control points within the stereo model. Maps thus have substantial uncertainties in absolute coordinates (latitude and longitude) and orientation (regional slope). Uncertainties in horizontal position can be controlled within limits by referring to the horizontal geodetic control nets of Davies and Berg (1971), Davies and Arthur (1973), and Davies et al. (1978), which have governed the compilation of shaded relief maps published by the U.S. Geological Survey.

Vertical control is a more severe problem for compilation of any topographic map that is less than global in scope. Global stereo imaging data did not exist before acquisition of HASSI, so the existing geodetic control nets were derived by calculations which treated the elevations of features as a fixed parameter, derived to first order from non-imaging data. Thus, local topographic maps have uncertainties of several to tens of km in the absolute value of the chosen datum and uncertainties on the order of a few tenths of a degree in the orientation of that datum. The topographic maps presented here are thus presented without an absolute vertical datum and with the reservation that regional slopes are uncertain to approximately $\pm 0.3^\circ$.

The other types of data which can be used to provide some level of vertical control to Mars topographic maps (earth-based radar ranging, spacecraft occultation, etc.) are described by Wu (1978). Unfortunately, no orbital radar altimetry has been acquired. The most accurate independent data have areal resolution far poorer than orbital imaging data, however, so only generalized global scale topography is well controlled. In addition, such data are not evenly distributed over the surface of Mars so large regions of the planet are entirely without vertical control. Resolution of this problem must await a global geodetic control net calculation combining HASSI stereo imaging with other types of data.

In limited equatorial regions the density of coverage and resolution of earth-based radar altimetry (Downs et al., 1975) is sufficient that these data might be used successfully to control regional topographic maps compiled from stereo imaging.

MAP COMPILATION TECHNIQUES

Stereo pairs of Viking Orbiter images were compiled into topographic maps of volcanic features presented here through the use of digital image measurement techniques developed for the Viking Orbiter Imaging Team by the staff of the Image Processing Laboratory, JPL under our direction. Most of the techniques involved are outlined by Ruiz et al. (1977), but we summarize and update salient features here.

There were two motives for developing a digital system for reduction of Viking Orbiter stereo images:

1. to speed map compilation and improve accuracy by working with the original digital image records inside a computer rather than converting those records to an analog film form before measurement, and
2. to develop portable software which would allow investigators not possessing stereo-plotters to quantitatively analyze spacecraft stereo imaging of other planets.

Point 1 was of particular concern for selecting landing sites for Viking. As events ran their course, however, both landing sites were selected on relatively flat terrain far from high relief features whose hazard could have been assessed from orbiter stereo images. Roughness at the scale of the lander vehicle itself constituted the principal hazard and this is far beyond the resolution of any orbiter image.

The portability of the software remains to be tested. A number of institutions, including our own, are establishing small-scale image processing facilities for planetary research. Attempts to perform digital photogrammetry will certainly be made.

A group of topographic mapping programs were written and exercised in an interactive image processing facility established at JPL. Within the limitations of manpower and facility time allocated to the Orbiter Imaging Team the programs have proven to be reasonable efficient tools for measuring topography on Mars. About thirty stereo pairs have been analyzed to compile rough topographic maps of a variety of features (Blasius, 1980). Data from nine of those maps are discussed here (Table 1).

The accuracy of the digital techniques has been verified to a practical level, although no superiority to stereo-plotter-based methods has been demonstrated, through comparison of two maps. Independently, two topographic maps of a portion of Candor Chasma were compiled from the same Viking data by using film positives on an AP/C stereo plotter (Wu, 1978, Figure 7) and by using the Viking digital photogrammetry software at IPL, JPL (Figure 1). Profiles AB and CD in Figure 1 allow direct comparison of the two maps. A nominal and a corrected profile are shown for AB on the IPL/PSI map; comparison should be made with the corrected profile. The correction applied removes the effects of displacements due to local relief within the topographic maps. The IPL software produces, as a final product, elevation contours overlayed on an orthographic projection of a Viking image (Figure 2). This projection assumes a triaxial ellipsoid shape for Mars but does not incorporate higher order features of the planet's topography. Having compiled

the topographic map of Figure 1 it is possible to make those corrections to an image data set to obtain a true orthophoto. For this paper corrections were figured manually using perspective geometry (Blasius, 1978) for the profiles in Figure 1. Only profile AB with its steep slopes required significant correction. All significant differences in the two profiles are explained by a simple rotation of one stereo model relative to the other. The model of Wu (1978) was oriented by arbitrarily fixing the elevations of three points (Wu, private communication); the digital map used spacecraft navigation data. The 1° and 2° relative rotations are explained by these procedures, which were necessitated by the lack of vertical geodetic control. Additional comparisons of our digital data with independent measurements of topography are made in Appendix A.

Digital topographic map compilation is conveniently broken down into nine steps:

1. select a stereo image pair,
2. rectify and scale identically both images,
3. measure parallax displacements,
4. compute elevations,
5. interpolate between elevation determinations to create a digital elevation map in the same format as a rectified image from Step 2,

6. contour the elevation map,
7. overlay the contours on a rectified image,
8. record on film the results of Steps 2, 3, 5, and 7,
9. compile an edited topographic map or set of profiles using the photographic products of Step 8.

Steps 1 and 9 are necessarily performed by the user cartographer/scientist while Steps 2 through 8 can be carried out by a scientist or trained technician. Steps 3 to 8 may be repeated, after consulting the user, to edit out bad data or make additional measurements to raise the quality of the four final digital topographic map products.

These steps are illustrated here with digital topographic map products compiled for the volcano Olympus Mons. A pair of images acquired by Viking Orbiter 1 on its 646th revolution of Mars was selected (Table 1).

Step 1. These images satisfied, among other criteria, the necessity that stereo pairs be acquired under similar lighting conditions and with similar resolution but with different viewing perspectives.

Step 2. The two images were rectified to an orthographic projection at a common center and at a scale of 800 m per pixel. The picture pair is shown in Figure 3A.

Step 3. The measurement of stereo images is performed in an interactive terminal facility time sharing on an IBM 360/65 computer (now upgraded to 370/158). The images are stored locally on a RAMTEK GX-100B digital storage device and displayed for the analyst on a CONRAC black-and-white monitor. Digital cursors generated by the RAMTEK are controlled by trackballs. An IMLAC CRT terminal is used to communicate with the central processor.

The procedure fundamentally consists of locating the left cursor on a feature whose parallax is to be measured and determining the position of the corresponding feature in the right picture using a cross-correlation algorithm. A visual vector representation of the parallax displacements is created on the monitor as the measurements are performed (as in Figure 4B). The selected feature may be varied in size to any square of dimension 2^n pixels, $n = 1, 2, \dots$. Most commonly 8×8 , 16×16 , and 32×32 pixel features have been used. It is also possible to define an array of regularly spaced points in the left picture and have the central computer systematically measure them all. The correlation algorithm acts by computing the Fourier transform of areas from both pictures, calculating the product of those transforms, and then finding the inverse transform to yield the cross correlation. Offsets

of the correlation maximum from the origin give corrections to the estimate of common features coordinates. Details of the cross-correlation algorithm are given by Ruiz et al. (1977).

In Step 4 a file of coordinates of corresponding features is transformed from the rectified image coordinate system to an idealized camera focal plan coordinate system. A program to determine a relative orientation from spacecraft orbital and navigational data (Benesh, 1978) is then applied to calculate x, y, z coordinates of each measured feature and then to transform those to horizontal and Mars radius coordinates.

The absolute value of Mars radius for any given feature is generally in error by a few to several tens of km due to uncertainties in camera orientation, but differences in elevation within a model can be accurate to the level of image spatial resolution. The maps compiled are thus accurate representations of relative topography but without geodetic control they generally are incorrect as to the absolute elevation of any point or as to regional slopes to better than approximately $\pm 0.3^{\circ}$.

In Step 5 the Mars radius values are used to create an image data file in the format of one rectified image where grey level is proportional to relative elevation and elevations between measured points have been filled in by interpolation (Figure 4C).

The grey level elevation image is contoured (Step 6) and overlaid on the rectified image (Step 7). The product is a contoured topographic photo-map such as Figure 3D.

Step 8. The final digital step is conversion of the four digital records of images in Figures 3A, B, C, and D into photographic hardcopy which can be used by a cartographer/scientist. This is done using a film recording device which accepts tapes written by the central computer.

Step 9 is the compilation of a final topographic map, profile, or other useful representation of the data. The maps presented in the next section were prepared by editing and smoothing the computer-generated contoured topographic maps while referring to the vector and grey level elevation displays and visually studying the stereo image pair.

MAPPING RESULTS

Results of digital analysis of nine stereo pairs of Viking Orbiter images are presented here. For three pairs the results are presented as contoured topographic maps (Step 9). For the other six data sets, which are mostly higher resolution, only general topographic characteristics of the imaged features are discussed. The interested reader is referred to the photographic map products which have been generated (column 5, Table 1) and are available from the National Space Science Data Center. A report (Blasius and Cutts, 1980), available from the authors, contains reproductions of these imaging data and detailed listings of coordinates and elevations for the three contoured topographic maps of volcanoes presented in this paper.

The three maps presented here were compiled from HASSI data, and each shows the topography of one to three entire central volcanic constructs at a contour interval of 1km. They are Figure 5, a map of Olympus Mons; Figure 6, a map of Elysium Mons and part of Albor Tholus; and Figure 7, a map of three smaller volcanoes of the Tharsis region. Also shown in each figure is an enhancement of one of the images used to compile the map.

OLYMPUS MONS

Olympus Mons (Figure 5) rises 20 to 23 km above surrounding terrains. Its flank slopes average about 4° . The total volume for the mountain is calculated to be $3.0 \pm 0.1 \times 10^6 \text{ km}^3$ (Table 2). In Appendix A this map, compiled from 692 separate elevation determinations, is compared to earlier independent point elevation studies of Olympus Mons. The horizontal datum for this map is a plane fitted to elevation measurements from areas around the perimeter of the shield. The resulting map is generally, symmetric and slopes resemble those found in independent geodetic analyses (See Appendix A). Dashed contours are used to indicate uncertain topography due to local low density of parallax measurements. Because of the low resolution of the images, high local slopes were not accurately

measured in areas such as the walls of the summit caldera and the face of the basal escarpment.

Variations in larger scale slopes on the volcano's flanks define an axis of rough symmetry running northwest-southeast through the summit caldera. South and east of the summit slopes are systematically steeper than toward the north and west (Table 3). Olympus Mons possesses a nearly ideal shield-like form on flanks where the basal scarp is greatly subdued or absent: a flattened summit, steeper upper slopes, and gradually shallowing lower slopes. To the north and west, where the basal scarp is prominent, flank slopes are relatively shallow immediately above the basal scarp. There may be a narrower zone of low slopes above the prominent reach of basal scarp to the southeast.

In general, flank slopes seem to correlate with flank morphology as described by Carr et al. (1977). The steep upper flanks are hummocky, terraced, and covered by thin flows. These grade into flatter lower flanks which are relatively smooth at a scale larger than a single flow width (1-2 km) or are crossed by long ridges thought to be tube-fed lava flows. This morphology is most common on the shallow flanks above the north and west basal scarp. A second type of lower flank, corresponding to steeper slopes,

is formed of lava fans, apparently tube-fed. Lava flows which can be traced back to an origin on the flanks of the shield extend for greatest distances to the northeast and southwest, beyond the most subdued reaches of basal scarp. It appears that enhanced lava flow eruption on those flanks has largely buried the basal scarp and greatly increased the breadth of the shield.

There are considerable geophysical implications arising from the existence of an enormous volcanic construct such as Olympus Mons. One aspect is the local modification of the Martian gravitational field. Sjogren (1979) reports Viking Orbiter 2 detected a + 300 mgal free air anomaly at 300 km altitude over Olympus Mons. He modeled this anomaly as a 600-km-diameter surface disk and derived a mass of $8.6 \text{ to } 8.8 \times 10^{21} \text{ gm}$. If this mass is attributed to the topographic relief mapped in Figure 5, then a mean density of $2.8 \text{ to } 3.0 \text{ gm/cm}^3$ is found. This is very dense compared to terrestrial basaltic shields. A bulk density of 2.3 gm/cm^3 accords well with gravity measurements across the Hawaiian Ridge and deep-well data on the island of Hawaii. Unvesiculated Hawaiian basalt magma has a column density of only about 2.8 gm/cm^3 at depth (Wollard, 1951 and Eaton and Murata, 1960). If the bulk density of Olympus Mons is similar to terrestrial shields the mountain cannot be simply

compensated by a low density root. Rather, a high density foundation seems indicated. The nature of this density anomaly may be illuminated by nearby surface features, lobes of mountainous or "grooved" terrain which form an aureole around Olympus Mons. Shoemaker and Blasius (1974) have suggested that much of the grooved terrain represents surface deformation over or exposures of shallow high density lopolithic intrusive bodies of basic composition. In addition to being the largest central volcanic construct known, Olympus Mons is also a geophysical anomaly on Mars. Though evidence above indicates the mountain is a largely uncompensated load on the Martian lithosphere, models of the three other very large central volcanoes in the Tharsis Volcanic Province indicate substantial compensation of topography (Smith et al., 1980).

ELYSIUM MONS

Elysium Mons, the larger volcano mapped in Figure 6A, rises 13 ± 0.5 km above surrounding terrains. Mean flank slopes of $4.4 \pm 0.2^\circ$ are not significantly different from those of Olympus Mons (Table 2). 280 separate point elevation determinations contributed to the map of Figure 6A. Although maximum slopes are not well defined by the 13 elevation measurements within 60 km of the summit, resulting in many dashed contours, the map suggests steepest slopes on a scale of ~ 10 km are around 18° compared to 12° on Olympus Mons (Table 3). The volcano's total volume is estimated to be $2.2 \pm 0.3 \times 10^5 \text{ km}^3$. The summit of the volcano lies

slightly south of its center of volume (Figure 6) suggesting a lobate extension to the north. Malin (1977) describes from Mariner 9 images a broad lobe of hummocky terrain extending over 200 km to the north of the volcano. In large part the 0-contour in Figure 6 encompasses that lobe, for the Viking mapping imaging is so superior to that of Mariner 9 that the volcano is now seen to have lateral dimensions, based on visible lava flows, of about 420 to 500 by 780 km, compared to a 170 km basal diameter estimated by Malin. Malin estimated local relief of Elysium Mons and arrived at a value of about 14 km.

Pike, et al. (1980) have plotted one partial (273 km) N-S profile of Elysium Mons using medium resolution Viking stereo images (846A18, 844A17). They found 12.5 km of relief across the northern flank, consistent with our map (Figure 6), but acknowledged the model may have been tilted by an arbitrary amount relative to a horizontal datum.

Malin (1977) also made a detailed comparison of the surface morphology of the summit region of Elysium Mons with the African shield volcano Emi Koussi. The two have many similarities--similar size summit calderas, containing smaller craters and irregular pits, and channel-like features heading at the caldera rims and tapering downslope. The slopes of Emi Koussi display numerous lava flows and cinder cones while the upper flanks of Elysium Mons are

characterized by irregular hummocks and numerous (mostly endogenic) craters. Emi Koussi is a 70-km-diameter shield with only about 2 km of relief and flank slopes of typically 2° to 5° . Though similar in size, the summit caldera of Emi Koussi is proportionately several times larger in diameter than that of Elysium Mons compared to overall volcano diameter.

Malin (1977) concluded Elysium Mons is most likely a composite volcano because of the steep estimated slopes, lack of visible lava flows, and abundant volcanic craters on its flanks. Our data confirm the existence of steep near summit slopes, but indicate low average slopes not inconsistent with a lava shield. High resolution Viking images (687A61-67) of the volcano's flank just to the west of the summit region show many low relief surface flows mostly less than 1 km in width. If the hummocky near-summit surface of the volcano is largely pyroclastic material, as suggested by Malin, this type of material may be volumetrically unimportant to the volcano as a whole. Perhaps there occurred a terminal phase of more silicic volcanism such as seems to mark the end of activity of Hawaiian shields (Eaton and Murata, 1960). Alternatively, interpretation of Elysium Mons as a composite volcano may be based upon a study of terrestrial volcano morphometry by Pike (1978). For large caldera

bearing constructs, slope steepness seems less useful than relative caldera size for separating lava shields from composite cones (Pike, 1978; Fig. 4). Elysium Mons has a proportionately smaller summit caldera (Fig. 6B) than Olympus Mons (Fig. 5B) or other great lava flow mantled shields.

ALBOR THOLUS

Also mapped in Figure 6A is the northern half of the volcano Albor Tholus. Local relief is about 3 km and flank slopes average about 5° (Table 2). There is a sharp break in slope where the volcano flank meets the surrounding plain to the north and west. A higher resolution image (Viking 846A21) shows hummocky flank surface textures end abruptly there also, but grade more gradually into surrounding plains to the southeast. These relationships indicate burial of the lower flanks of Albor Tholus at least toward the northwest, probably by lava flows from up the regional slope, the direction of Elysium Mons (Christensen, 1975 and USGS, 1976). Beneath a partial cover of later flows, Albor Tholus may be a much broader shield-like construct.

Pike et al. (1980) report an independent determination of the relief of Albor Tholus using the Viking image 846A21. They find the volcano has 5 km of relief, but do not specify the technique used. Presumably it is

photometric though not a shadow measurement. No confidence limits are given on this determination, but the nominal value of 5 km far exceeds our estimate of 3 ± 0.5 km.

CERAUNIUS THOLUS

Ceraunius Tholus is a 115-km-diameter volcanic cone mapped in Figure 7A. This map compiled from 501 separate elevation determinations also shows two other large central volcanic constructs which are described in following sections. This volcano rises 6 ± 0.5 km above the surrounding plain and has average flank slopes of $8.9 \pm 0.7^\circ$ (Table 2). This is a significantly steeper construct than Olympus or Elysium Mons, and the topographic maps indicate that slopes are more nearly uniform. A gradual transition to very shallow lower flank slopes is absent, so this volcano is probably more accurately characterized as a cone rather than a shield.

Pike, et al. (1980) report two profiles (NW-SE, NE-SW) of Ceraunius Tholus compiled from the Viking HASSI Stereo pair (701A08, 816A09). They find the volcano to have 5.15 km of relief, but qualify the result by acknowledging the model may be arbitrarily tilted. The volcano image is just at the edge of one image so profiles couldn't be extended well out into the plains in all directions. Given this qualification, our results (Table 2) are in good agreement with those of Pike, et al.

The flank slopes of Ceraunius Tholus do fall within the normal range for terrestrial basaltic shields. If shallower lower slopes of the construct have been buried by later plains deposits, as suggested above for a portion of Albor Tholus, then Ceraunius may be just a steeper-than-average shield volcano. Higher resolution Viking images (516A22,24; 662A55-61) support the hypothesis of partial burial. Hummocky and channeled flank slopes are abruptly cut-off by flat plains of very low relief. The few features visible on the plains seem to be margins of broad thin lava flows possibly originating to the south of the area of Figure 7.

An alternative interpretation of the plains has been recently offered by Reimers and Komar (1979). They point out that the flanks of this volcano, and its neighbor Uranus Tholus, are relatively steep and channeled and interpret them as tuff cones or composite volcanoes channeled by explosive volcanic density currents. Excessively high relief and slope estimates of 9 to 11 km and 10° to 12° for Ceraunius Tholus, from apparent shadows, at least partially motivated this interpretation. Reimers and Komar interpret the abrupt disappearance of flank channels at the base of the volcanoes as due to burial beneath smooth ash deposits from the mobile flows which cascaded down the volcano flanks. No contact between the supposed ash deposits and plains lava flow deposits has been discerned by us in the images, however.

The new topographic data presented here allows a smaller role of explosive volcanism in the construction of Ceraunius Tholus than that which is suggested by Reimers and Komar (1979). Their arguments about the morphology of flank channels is compelling, however, so a special geologic process such as a terminal stage of explosive volcanism seems to be required. Earlier in its history, Ceraunius Tholus may have been a lava shield or a composite cone. We interpret the embaying plains as a later lava flood deposit not originating from the central volcanoes mapped in Figure 7A.

URANIUS THOLUS

Uranus Tholus is a 60-km-diameter cone (Figures 7A and B) rising 1.5 to 2.5 km from the same plain as Ceraunius Tholus. It also has many characteristics in common with its neighbor, flank slopes, $7.1 \pm 1.8^\circ$ (Table 2), are distinctly steeper than those of the broad shields. On the surface of the cone is a radial pattern of channels. The character of the surrounding plains and its relationship to the volcano's flank are the same as for Ceraunius Tholus. Reimers and Komar (1979) interpreted both volcanoes in the same way, as described above, even though they estimated the flank slopes of Uranus Tholus to be much shallower than those of Ceraunius Tholus, only 5° to 6° as compared to 10° to 12° .

Pike, et al. (1980) published two profiles (NW-SE, WE-SW) of Uranus Tholus compiled from the Viking HASSI stereo pair (701A08, 816A09). They show the volcano to rise 2.45 km above the surrounding plain. As with the results they report for Ceraunius Tholus, possible tilt of the stereo model implies an unestimated uncertainty must be attached to this measurement. It is in good agreement with our estimate of relief of 1.5 to 2.5 km.

Our interpretation of the morphology of Uranus Tholus is the same as that of Ceraunius Tholus, i.e., it is possibly a shield or composite cone which went through a terminal phase of explosive volcanism and was then partially buried by lava flood deposits.

URANIUS PATERA

To the east of Uranus Tholus is an unmistakable lava shield volcano, Uranus Patera (Figure 7) with an enormous summit caldera comparable in size to that of Olympus Mons. Its mean basal diameter is about 240 km and average flank slopes are $2.7 \pm 0.7^\circ$. Local relief is, perhaps surprisingly, only 1.5 to 2.5 km (Table 2). Pike et al. (1980) report relief of 1.63 km, in good agreement with our results, from two profiles compiled from HASSI stereo pair (701A08, 816A09). They acknowledge an uncertainty in relief due to unconstrained tilt of the stereo model but do not attempt to estimate it.

To the west and north this construct rises from the same plains as its two smaller neighbors. Again, photogeologic evidence near the contact of the flank with those plains indicates embayment by lava flood deposits. Higher resolution Viking imaging (516A21,22) of north and west margins shows a hummocky flank surface largely covered by lava flows terminating abruptly at the plains contact. To the east the onlap of plains flows is even more obvious. Viking images 857A43-46 show distinct broad lava flows of the plains embaying the hummocky volcano flank, and a set of parallel graben which cut the volcano flank disappear by gradually shallowing as if flooded across the contact with the plains. The sharp termination of steep channeled and hummocky flanks against smooth plains is not the primary morphology of any of the three central volcanoes of Figure 7. Uranus Patera is clearly a distinct landform from the other two volcanoes, however. The flank morphology is much like that of Olympus Mons with no clear evidence of blanketing or channeling. As to how the original relief of Uranus Patera might compare with that of Olympus Mons or other great shields we can only guess; a study of regional stratigraphy might constrain estimates, however.

OTHER TOPOGRAPHIC DATA FOR CENTRAL VOLCANOES

Also listed in Table 2 are summary data drawn from other digital topographic map products made from Viking Orbiter images of volcanic landforms. Some higher resolution data of the summit region of Olympus Mons (46B09, 46B31, 46B11; Table 1) has been reduced. The principal result is that walls of the summit caldera range in height from about 1 to 3 km (Table 2).

A portion of the summit and west flank of the shield Arsia Mons has been analyzed from low resolution images 571A50 and 574A48. These data were not compiled into a map because no obvious datum (such as a basal plain) was available for referencing elevations and slopes. Apparent volcano relief of 19 km and flank slopes averaging above 2° do not, however, differ significantly from an earlier also partial map of Arsia Mons (Wu, et al., 1973).

Very high resolution stereo images of the summit caldera of Arsia Mons (422A34, 14, 35, 15; Table 1) have also been analyzed. These show a portion of the faulted caldera rim rising 250 to 350 m above the flooded floor and several low shield-like constructs on the caldera floor (Carr, et al. 1977). These small parasitic volcanoes have only 100 to 200 m of relief and flank slopes of less than about 2.5° .

Finally, we have reduced some topographic data for Hadriaca Patera, a much older and very different form of central volcano that is characterized by a coarse radial pattern of lava flows and channels (Carr, 1973 and

Masursky, et al. 1977). Only the caldera rim and north flank were mapped, so slopes are rather uncertain, but nominal values of local relief and flank slopes are ~ 1 km and $\leq 1^\circ$, respectively. The apparent very low relief of this class of old central volcano has been discussed by Carr (1976a,b). He notes a general trend of decreasing volcano relief with increasing age and suggests as possible explanations - thickening with time of the lithosphere, increasing the hydrostatic head on erupted lava, subsidence of volcanic constructs over time, systematic changes in the chemistry and physical properties of lavas over Martian history. Accurate topographic data can contribute to a better understanding of these and other issues of Martian thermal evolution.

FINAL REMARKS

We have attempted to explain and demonstrate the usefulness of digital photogrammetric techniques developed at the Image Processing Laboratory, JPL, for Viking Orbiter data. The resulting data can contribute significantly to the geological and geophysical interpretation of volcanic constructs. Quantitative data from stereo imaging presented here differ in some instances from those of other authors who relied on identification of shadows or other photometric techniques for relief data. Among the large volcanoes examined, several thought by earlier investigators

to be probable composite or pyroclastic constructs now seem less likely to be so because average flank slopes are less than earlier estimates and abrupt topographic and morphologic boundaries are not primary but due to partial burial of the original cone or shield. These features may all have been shield volcanoes built almost entirely of fluid lava flows. In some cases a late stage of mixed or explosive volcanism may have modified surface morphology considerably without contributing greatly to the total volume of the volcanic construct.

Research areas other than volcanology could also benefit from quantitative analysis of high quality Viking stereo imaging. We are currently working on the stratigraphy of polar layered deposits. Detailed crater morphometry studies are possible. Using HASSI data the gradients of large martian channels can be determined and the lithospheric structure of Mars beneath rift valleys and impact basins can be modeled from high resolution gravity data. We hope to see this wealth of data more fully exploited in the future.

Existing computer stereo techniques can be significantly streamlined and the potential exists for measurements of improved height accuracy and spatial resolution. The programs described here can be adapted to work on smaller computers and specialized hardware which is becoming available at low cost will permit the researcher to efficiently exploit the potential of the Viking Orbiter stereo data set.

ACKNOWLEDGEMENTS

The data presented in this paper were several years in compilation. The authors are particularly grateful to their analysts at the Image Processing Laboratory who performed digital processing and assisted with system development. In chronological order, they were Margaret Power, Jenny Han, Andrew Howell, David Glackin and Steve Friedman. Their supervisors, Ruben Ruiz and Dennis Elliott, were also very helpful. Jean Lorre of IPL designed and has maintained the digital photogrammetry software. Milosh Benesh of JPL applied classical photogrammetric theory to the novel geometry of Viking Orbiter cameras and navigation data (Benesh, 1978). The Viking Orbiter Imaging Team and Team Leader Michael Carr were supportive of our efforts to gather data, develop software, and reduce data through Primary and Extended Missions. Finally, extra thanks are due to Conway Snyder. As Project Scientist he helped us find resources to acquire and reduce the high altitude stereo data represented by maps published here. The work reported here was supported by Jet Propulsion Laboratory Contract 954149 covering Viking Project tasks, NASA contract NASW3051 covering lunar and planetary data synthesis tasks, and NASA contract NASW3268 covering Mars Data Analysis Program tasks. Discussions within the NASA-sponsored Tharsis Working Group chaired by Roger Phillips motivated much of this work.

REFERENCES

- Benesh, M., 1978, Viking Orbiter Stereophotogrammetry, Photogram. Eng. Rem. Sens., 44, 265.
- Blasius, K.R., 1973, A Study of Martian Topography by Analytic Photogrammetry, J. Geophys. Res., 78, 4411-4423.
- Blasius, K.R., 1981, Index of Viking Orbiter Digital Topographic Map Products Produced at the Image Processing Laboratory, JPL and Planetary Science Institute, Pasadena, in preparation.
- Blasius, K.R. and Cutts, J.A., 1980, Digital Topographic Data for Six Martian Volcanoes Derived from Viking High Altitude Stereo Imaging, Planetary Science Inst. Report, available from authors.
- Blasius, R.R., Vetrone, A.V., and Martin, M.D., 1980, Viking Orbiter Stereo Imaging Catalog, NASA Contractor Report 3277, 302 p.
- Carr, M.H., 1973, Volcanism on Mars, J. Geophys. Res., 78, 4049-4062.
- Carr, M.H., 1976a, Elevation of Martian Volcanoes as a Function of Age, in Reports of Accomplishments of Planetary Program, NASA TMX-3364, p. 152-153.
- Carr, M.H., 1976b, Changes in Height of Martian Volcanoes with Time, Geol. Romana, 15, p. 421-422.
- Carr, M.H., Blasius, K.R., Greeley, R., Guest, J.E., and Murray, J.B., 1977, Some Martian Volcanic Features as Viewed from the Viking Orbiters, J. Geophys. Res., 82, 3985-4015.
- Christensen, E.J., 1975, Martian Topography Derived from Occultation, Radar, Spectral, and Optical Measurements, J. Geophys. Res., 80, 2909-2913.

Davies, M.E., and Arthur, D.W.G., 1973, Martian Surfaces Coordinates, J. Geophys. Res., 78, 4355.

Davies, M.E., and Berg, R.A., 1971, A Preliminary Control Net of Mars., J. Geophys. Res., 76, 373.

Davies, M.E., Katayama, F.Y., and Roth, J.A. 1978, Control Net of Mars: February 1978, RAND Report R-2309-NASA, 91.

Downs, G.S., Reichley, P.E. and Green, R.R., 1975, Radar Measurements of Martian Topography and Surface Properties, The 1971 and 1973 Oppositions, Icarus, 26, 273-312.

Eaton, J.P., and Murata, K.J., 1960, How Volcanoes Grow, Science, 132, 925-938.

Malin, M.E., 1977, Comparison of Volcanic Features of Elysium (Mars) and Tibesti (Earth), GSA Bulletin, 86, 908-919.

Masursky, H., Boyce, J.C., Dial, A.L., Schaber, G.G., and Strobell, M.E., 1977, Classification and Time of Formation of Martian Channels Based on Viking Data, J. Geophys. Res., 82, 4016-4038.

Pike, R.J., 1978, Volcanoes on the Inner Planets: Some Preliminary Comparisons of Gross Topography, Proc. Lunar Planet. Sci. Conf. 9th, p. 3239-3273.

Pike, R.J., Jordan, R., Schafer, F.J., 1980, Quantitative Morphology of Volcanoes: Recent Results for Earth and Mars (abs.), in Reports of Planetary Geology Program, 1979-1980, NASA TM81776, p. 192-194.

Reimers, C.E., and Komar, P.D., 1973, Evidence for Explosive Volcanic Density Currents on Certain Martian Volcanoes, Icarus, 39, 88-110.

Ruiz, R.M., Elliott, D.A., Yagi, G.M., Pomphrey, R.B., Power, M.A., Farrell, K.W., Lorre, J.J., Benton, W.D., Dewar, R.W., and Cullen, L.E., 1977, IPL Processing of the Viking Orbiter Images of Mars, J. Geophys. Res., 82, 4180-4202.

Shoemaker, E.M. and Blasius, K.R., 1974, Geology and Geomorphology of Martian Shield Volcanoes, Final Report to NASA for Grant NGR05-002-302, 205.

Sjogren, W.L., 1979, Mars Gravity: High Resolution Results from Viking Orbiter 2, Science, 203, 1006-1009.

Smith, J.C., Phillips, R.J., Ritke, S., 1980, An Analysis of Martian Gravity Over Three Shield Volcanoes (abs.), in Reports of Planetary Geology Program, 1979-1980, NASA TM-81776, p. 79.

U.S.G.S., 1976, Topographic Map of Mars, M25M 3RMC.

Wollard, G.P., 1951, A Gravity Reconnaissance of the Island of Oahu, Trans. Am. Geophys. Union, 32, 358-368.

Wu, S.S.C., 1978, Mars Synthetic Topographic Mapping, Icarus, 33, 417-440.

Wu, S.S.C., Schafer, F.J., Nakata, G.M., Jordan, R., and Blasius, K.R., 1973, Photogrammetric Evaluation of Mariner 9 Photography, J. Geophys. Res., 78, 4405-4423.

Table 1

Martian Volcano Topography Data from Viking Orbiter Stereo Imaging

Stereo Image Pair	Features	Input Image Resolution	Compiled Map Vertical Resolution	Digitally Derived Photogrammetric Data (Viking IPL Negative Numbers)
646A71, 646A28	Olympus Mons 19.3°N, 134.6°W	800 m/pixel	± 500 m	80/09/18/214929, 80/09/18/222104, 80/09/18/223539
729A01, 783A47	Elysium Mons, Albor Tholus 21.8°N, 211.7°W	600 m/pixel	± 500 m	80/09/26/102812, 80/09/26/111217, 80/09/26/113204
759A73, 701A08	Ceraunius Tholus, Uranus Tholus, Uranus Patera 24.6°N, 93.2°W	600 m/pixel	± 500 m	80/09/26/105524, 80/09/26/113434, 80/09/26/114544
87A04, 106A08	Hadriaca Patera 28°S, 125°W	230 m/pixel	-	78/04/17/171154, 171440, 171747
571A50, 574A48	NW Arsia Mons 7°S, 125°W	700 m/pixel	-	78/07/31/181912, 184928, 190639
46B09, 46B31	Olympus Mons, Summit Caldera 18.5°N, 133.5°W	125 m/pixel	-	77/04/20/003847, 003931, 004017
46B11, 46B31	Olympus Mons, Summit Caldera 18.5°N, 133.5°W	125 m/pixel	-	77/04/15/202301, 203106, 203531
422A34, 422A14	Arsia Mons, Summit Caldera Rim 8.3°S, 119.9°W	40 m/pixel	-	78/04/15/194223, 200224, 201202
422A35, 422A15	Arsia Mons, Summit Caldera Central Floor 9.1°S, 119.8°W	40 m/pixel	-	78/04/15/203817, 21042, 211550

TABLE 2: TOPOGRAPHIC CHARACTERISTICS OF SOME MARTIAN VOLCANIC FEATURES

Feature	Stereo Data	Image Resolution	Local Relief	Volume	Approx. Mean Flank Slope ⑤
Olympus Mons: shield	646A71, 646A28	800 m/pixel	20 to 23 ± 0.5 km	$3.0 \pm 0.1 \times 10^6 \text{ km}^3$	① 3.2 to $5.6 \pm 0.1^\circ$
summit caldera	46B09, 46B31, 46B11, 46B31	125 m/pixel	2-3 km		
Elysium Mons: shield	729A01, 783A47	600 m/pixel	$13 \pm 0.5 \text{ km}$	$2.2 \pm 0.3 \times 10^5 \text{ km}^3$	$4.4 \pm 0.2^\circ$
Albor Tholus: shield	729A01, 783A47	600 m/pixel	② $3 \pm 0.5 \text{ km}$	② $1.3 \pm 0.2 \times 10^4 \text{ km}^3$	② $5.3 \pm 0.9^\circ$
Ceraunius Tholus: shield	759A73, 701A08	600 m/pixel	$6 \pm 0.6 \text{ km}$	$7.8 \pm 1.1 \times 10^3 \text{ km}^3$	$8.9 \pm 0.7^\circ$
Uranus Tholus: shield	759A73, 701A08	600 m/pixel	$2 \pm 0.5 \text{ km}$	$9.1 \pm 1.4 \times 10^2 \text{ km}^3$	$7.1 \pm 1.8^\circ$
Uranus Patera: shield	759A73, 701A08	600 m/pixel	$2 \pm 0.5 \text{ km}$	$9.0 \pm 2.0 \times 10^3 \text{ km}^3$	$2.7 \pm 0.7^\circ$
Arsia Mons: shield	571A50, 574A48	700 m/pixel	③ ~19 km		2.1° (N.W. flank, over 500 km)
summit caldera rim	422A34, 422A14	40 m/pixel	~25-35 km		
parasitic shield within caldera	422A35, 422A15	40 m/pixel	~1-2 km		~2.5°
Hadriaca Patera	87A04, 106A08	230 m/pixel	④ ~1 km		~1° (to 50 km from crater rim)

① Including basal scarp

② Only the northern half of Albor Tholus was mapped. See Figure 6.

③ Only northwest flank of Arsia Mons was mapped.

④ Only crater rim and N. flank of volcano were mapped.

⑤ Stated errors are formal errors based on the uncertainty in the determination of volcano relief; the uncertainty in horizontal datum may increase these values in some cases.

TABLE 3:

FLANK SLOPES ON OLYMPUS MONE

From Summit To:	Range of Slopes Excluding Basal Scarp	Mean Slope	Mean Slope Above Basal Scarp
N	1° to 12°	4.0 \pm 0.1°	3.5 \pm 0.1°
S	2° to 11°	4.8 \pm 0.1°	--
E	3° to 12°	4.8 \pm 0.1°	4.7 \pm 0.1°
W	1° to 7°	3.2 \pm 0.1°	3.3 \pm 0.1°
NW	2° to 7°	3.5 \pm 0.1°	2.9 \pm 0.1°
SE	2° to 10°	5.6 \pm 0.1°	5.2 \pm 0.2°

FIGURE CAPTIONS

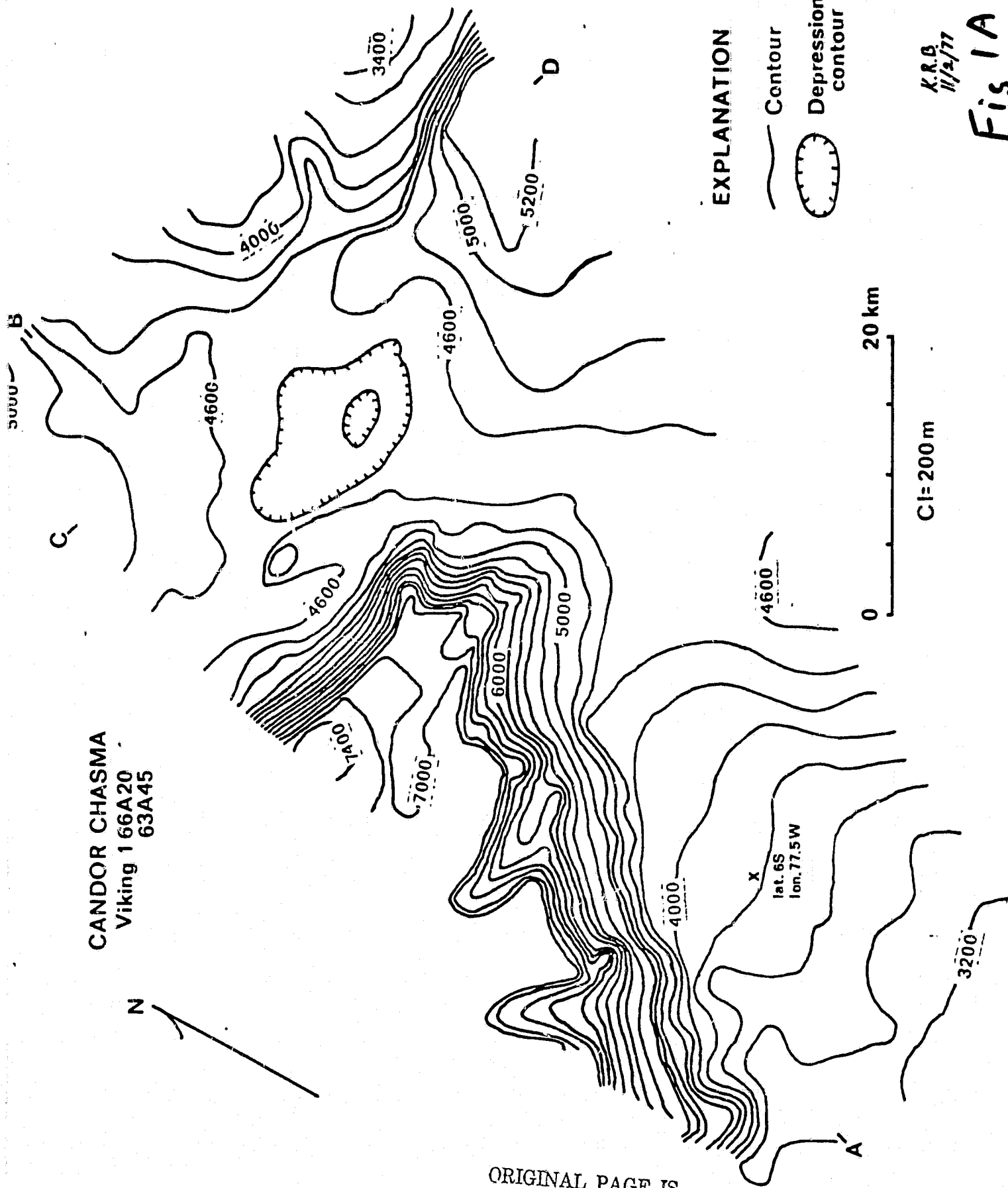
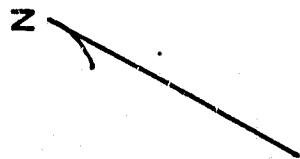
1. A. Topographic maps of a portion of the martian trough Candor Chasma. This map was compiled using digitally derived photogrammetric data as described in this paper. It is presented for comparison with a map of the same area compiled from the same Viking images using an AP/C plotter (Fig. 7 of Wu, 1978).
 - B. A comparison of topographic profiles between points (A,B) and (C,D) indicated in Figure 1A. The "Corrected" profile AB is an adjustment of our data to a true orthographic perspective as described in the text. The maps agree except for rotations of $\sim 1^\circ$ and $\sim 2^\circ$, which are not unexpected as no vertical geodetic control now exists in this area of Mars.

2. Digitally derived topography for Candor Chasma represented by 200m elevation contours, overlaid on Viking Orbiter image 53A45. The image has been rectified to a pseudo-orthographic perspective (no allowance has been made for the presence of local relief). The final map of Fig. 1A was based in large part upon this product of digital photogrammetry.

3. A. Stereo pair of Olympus Mons rectified to the same pseudo-orthographic projection. (Viking Orbiter frames 646A71, left and 646A28, right).
- B. Vector display indicating results of parallax measurements attempted on rectified stereo pair of Figure 3A.
- C. Grey level display of elevations calculated from parallax measurements in Figure 3B and interpolated. The base of the volcano was arbitrarily set to be approximately level.
- D. Elevations (represented in Figure 3C) have been contoured at C.I. = 1km and the contours overlaid on rectified image 646A28.
4. Analyst working environment at Image Processing Laboratory, JPL, for digital topographic mapping.
5. A. Topographic map of Olympus Mons with a contour interval of 1km. Placement of dashed contours is quite uncertain due to sparse measurements.
- B. Viking Orbiter image 646A28 (roll/frame = M3036-008) showing the area of the map in Figure 5A.
6. A. Topographic map of Elysium Mons and the north half of Albor Tholus. C.I. = 1km.

- B. Viking Orbiter image 729A01 (roll/frame = M3203-001)
showing the area mapped in Figure 6A.
-
- 7. A. Topographic map of Ceraunius Tholus (large cone),
Uranus Tholus (small cone to the south), and
Uranus Patera (broad shield to the east).
C.I. = 1km, supplementary contours at 500m.
 - B. Viking Orbiter image 701A08 (roll/frame = M3141-008)
showing the area mapped in Figure 7A.

CANDOR CHASMA
Viking 1 66A20
63A45



EXPLANATION

- Contour
- ⊖ Depression contour

K.R.B.
11/2/77

Fig 1A

ORIGINAL PAGE IS
OF POOR QUALITY

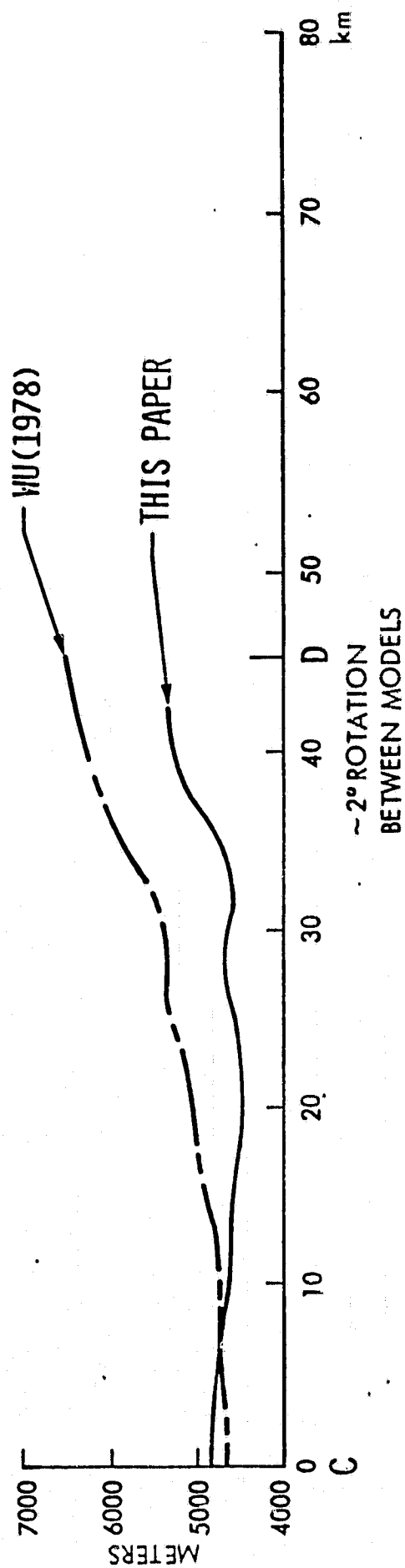
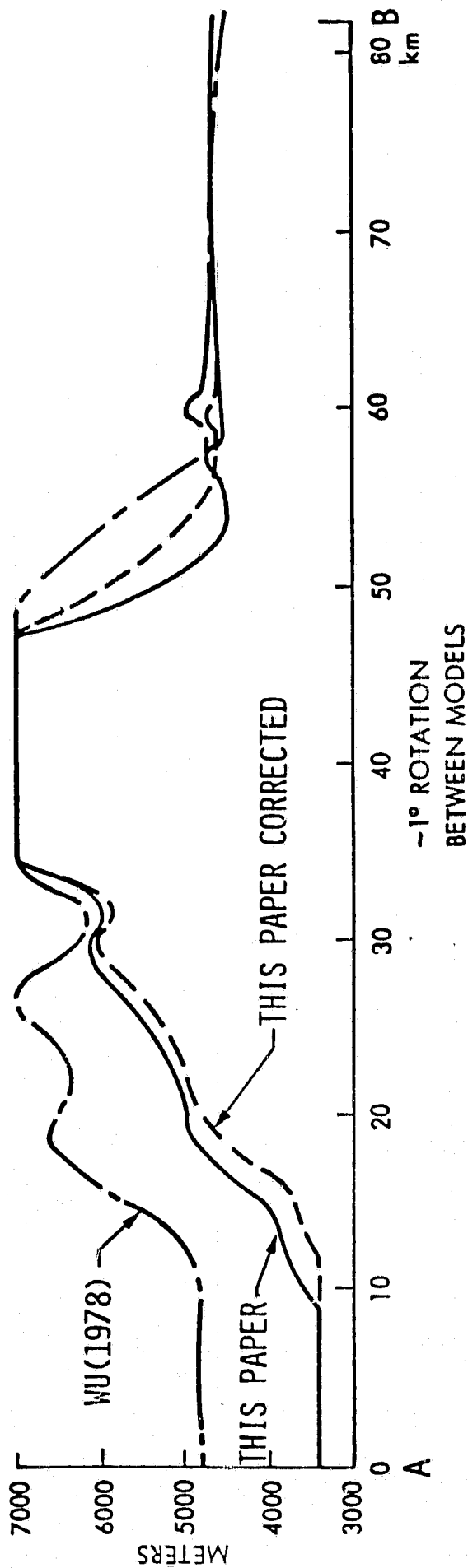
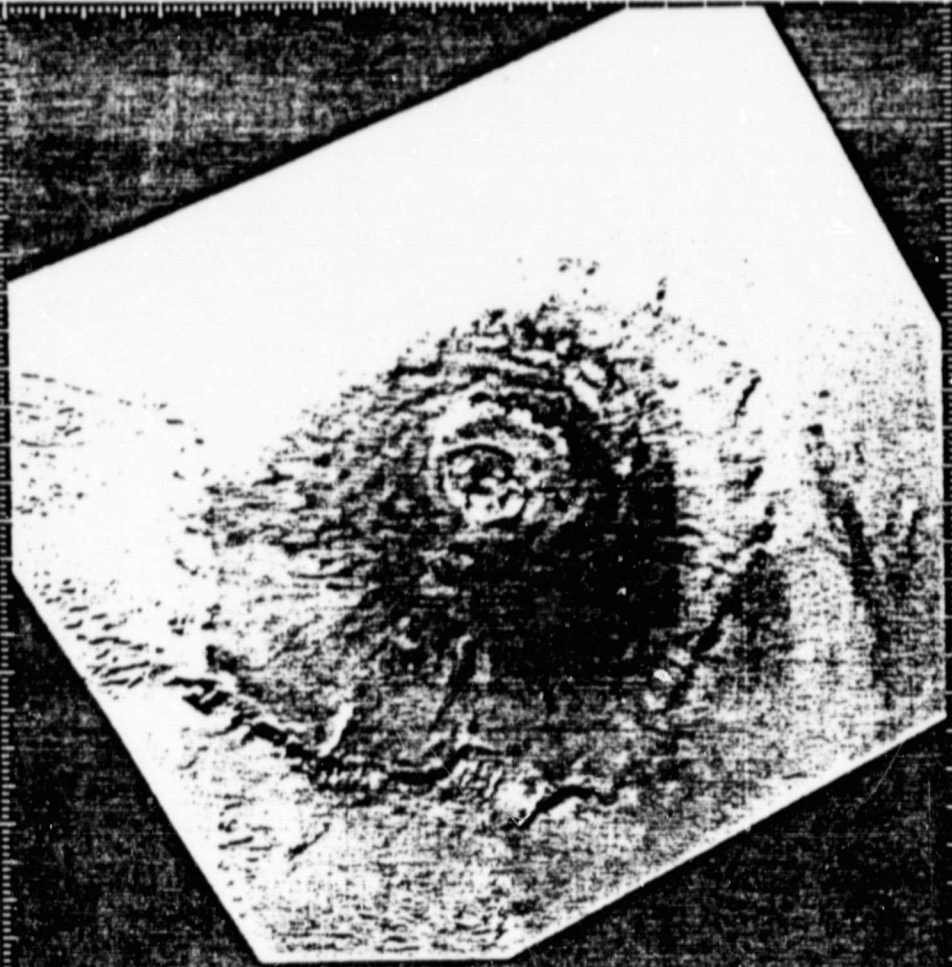


Fig 2



ORIGINAL PAGE IS
OF POOR QUALITY



STEREO PAIR LEFT PICNO= 646A71 FSC=38319510
 RIGHT PICNO= 646A28 FSC=38317901

SCALE=800 METERS PER PIXEL
 LOCATION= 19.3 DEGREES LATITUDE, 134.6 DEGREES WEST LONGITUDE
 NORTH AZIMUTH= 0. DEGREES CLOCKWISE FROM UP
 GAUSSIAN STRETCH
 OPWASK - STRETCH

IPL PIC ID 80/09/18/218734 LEC/13055X
 JPL IMAGE PROCESSING LABORATORY

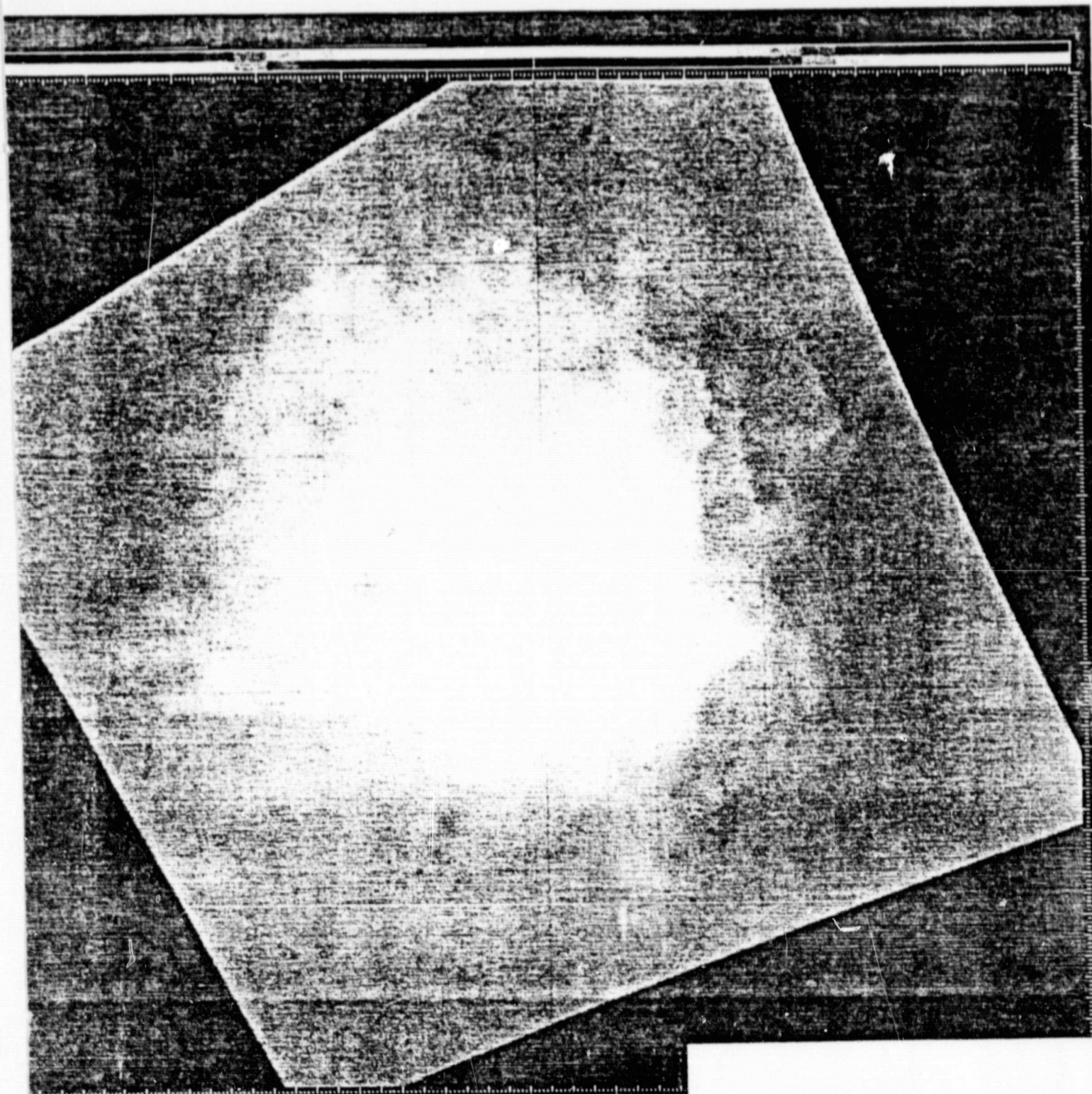
Fig. 3A

ORIGINAL PAGE
OF POOR QUALITY

Fig. 3b

PARALLAX DISPLACEMENTS EXAGGERATED 10X
STEREO PAIR/PICNOS= 646A71, 646A28
DIFFPIC - STRETCH

JPL-PIC-10 80/09/18/214929 LEC/T3055X
JPL IMAGE PROCESSING LABORATORY



TOPOGRAPHIC MAP
RIGHT=HIGH, DARK=LOW
STEREO PAIR PICNDS= 646A71, 646A28
RELATIVE BRIGHTNESS ADJUSTED WITH POLYFIT
STRETCH 46-206-STRETCH

Fig. 3c

[IPL PIC ID 80/09/18/222104] LEC/I3055X
JPL IMAGE PROCESSING LABORATORY

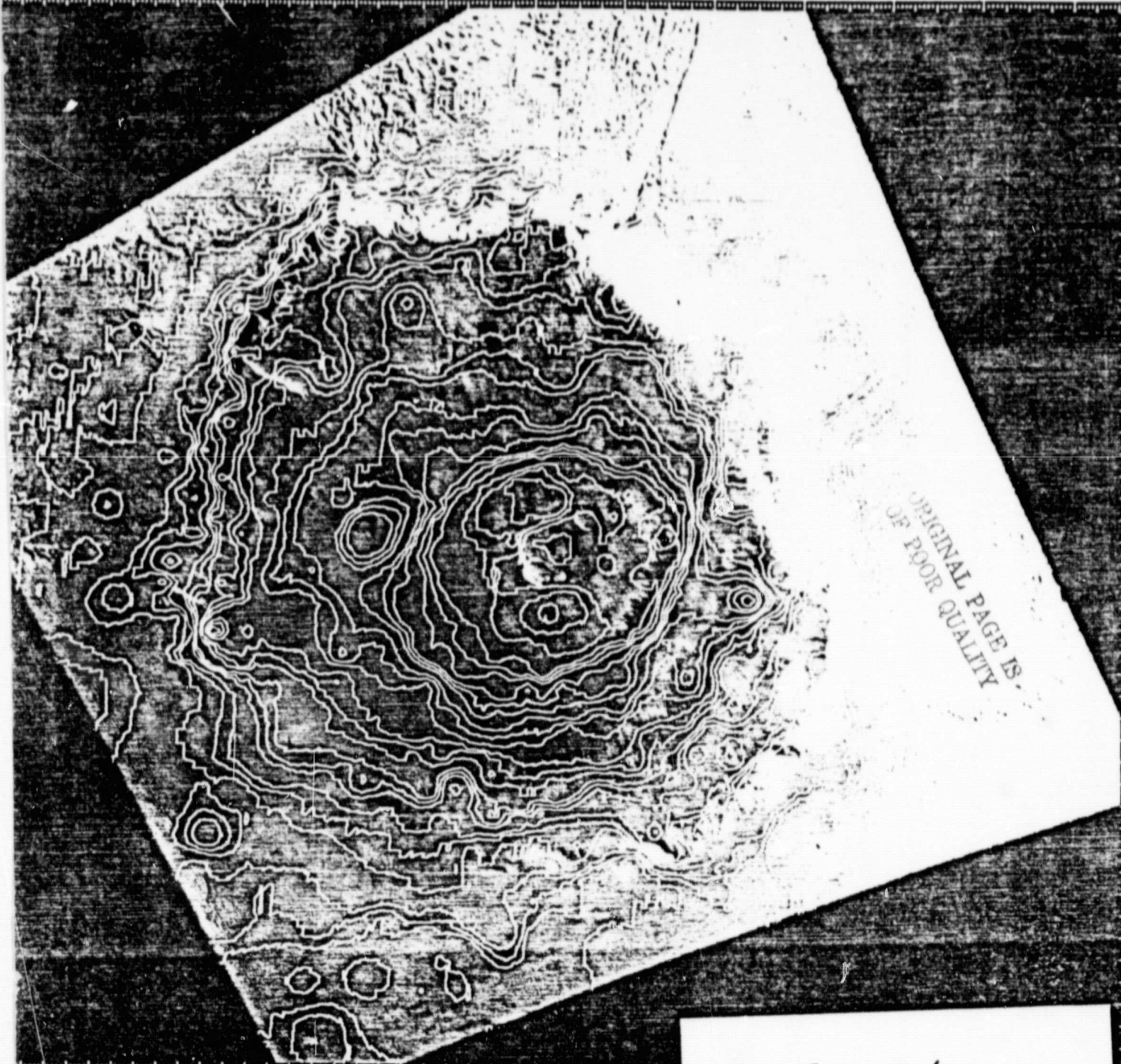


Fig. 3d

TOPOGRAPHIC MAP CONTOUR INTERVAL=1000 METERS
SCALE=800 METERS PER PIXEL
STEREO PAIR PICNOS= 646A71, 646A28
PHOTOGRAPHIC PHOTOBASE FROM PICNO 646A28
STRETCH

IPL PIC ID 80/09/18/223539 LEC/T3055X
JPL IMAGE PROCESSING LABORATORY

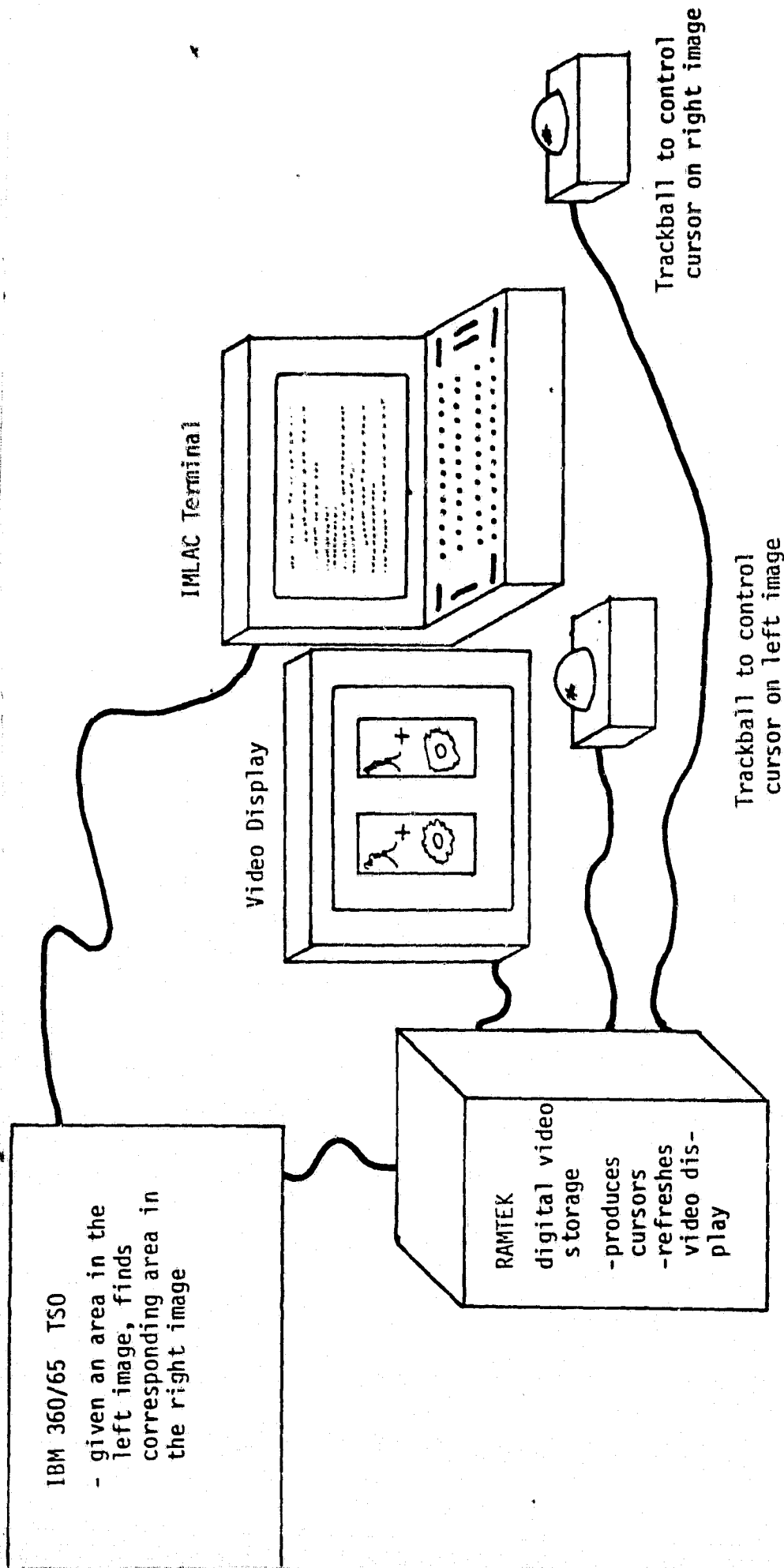


Fig. 4

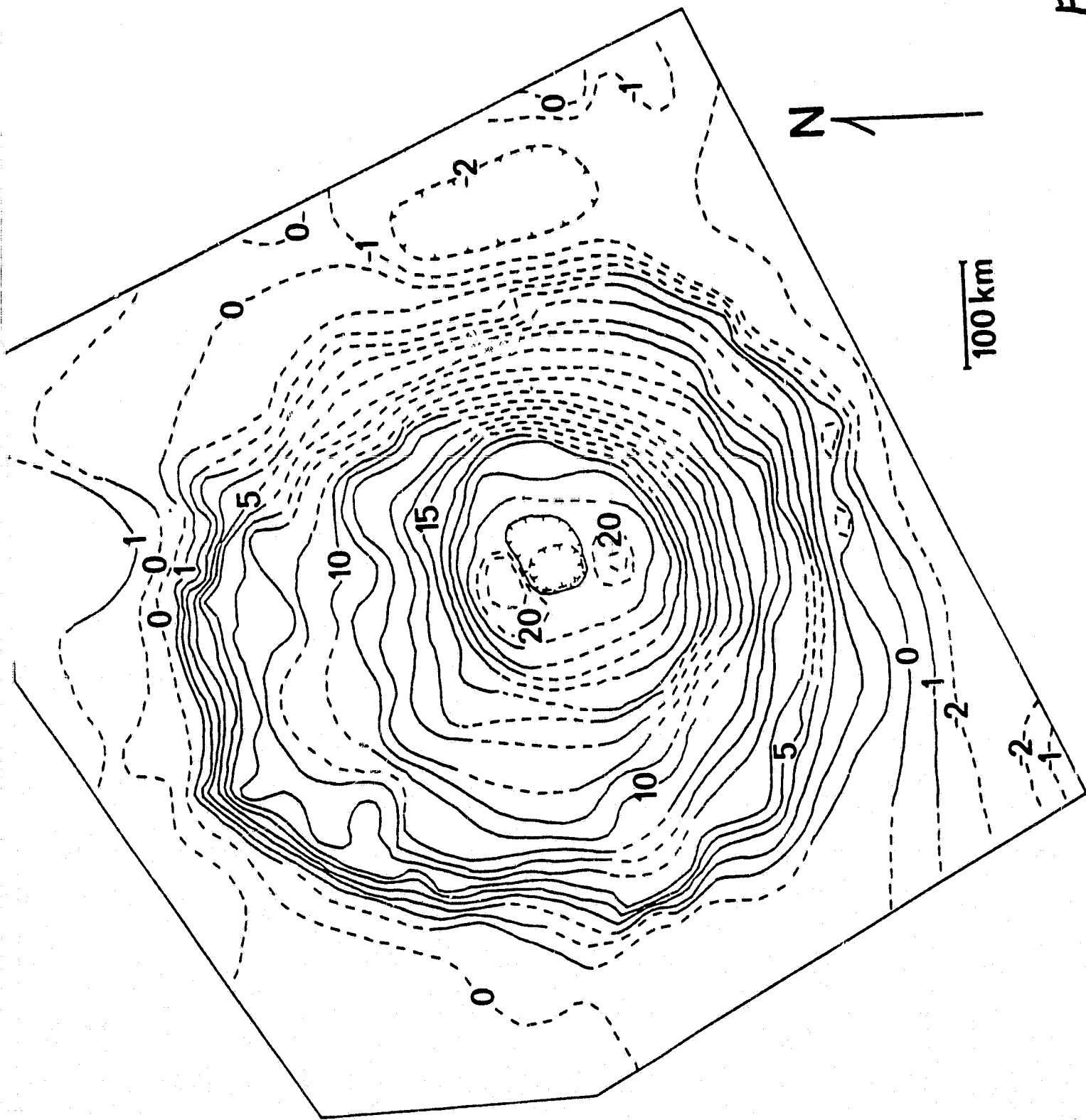
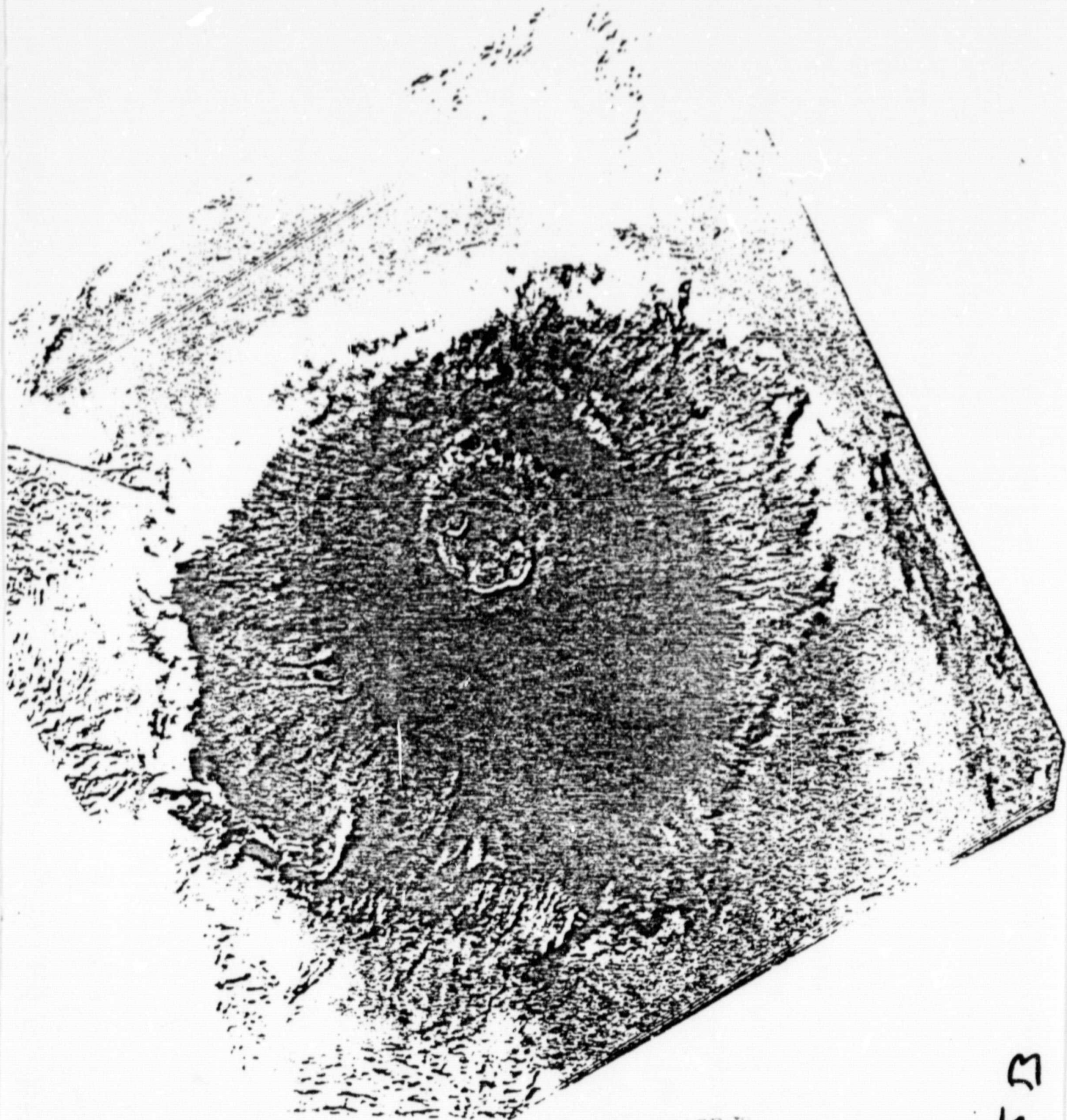


Fig. 5A



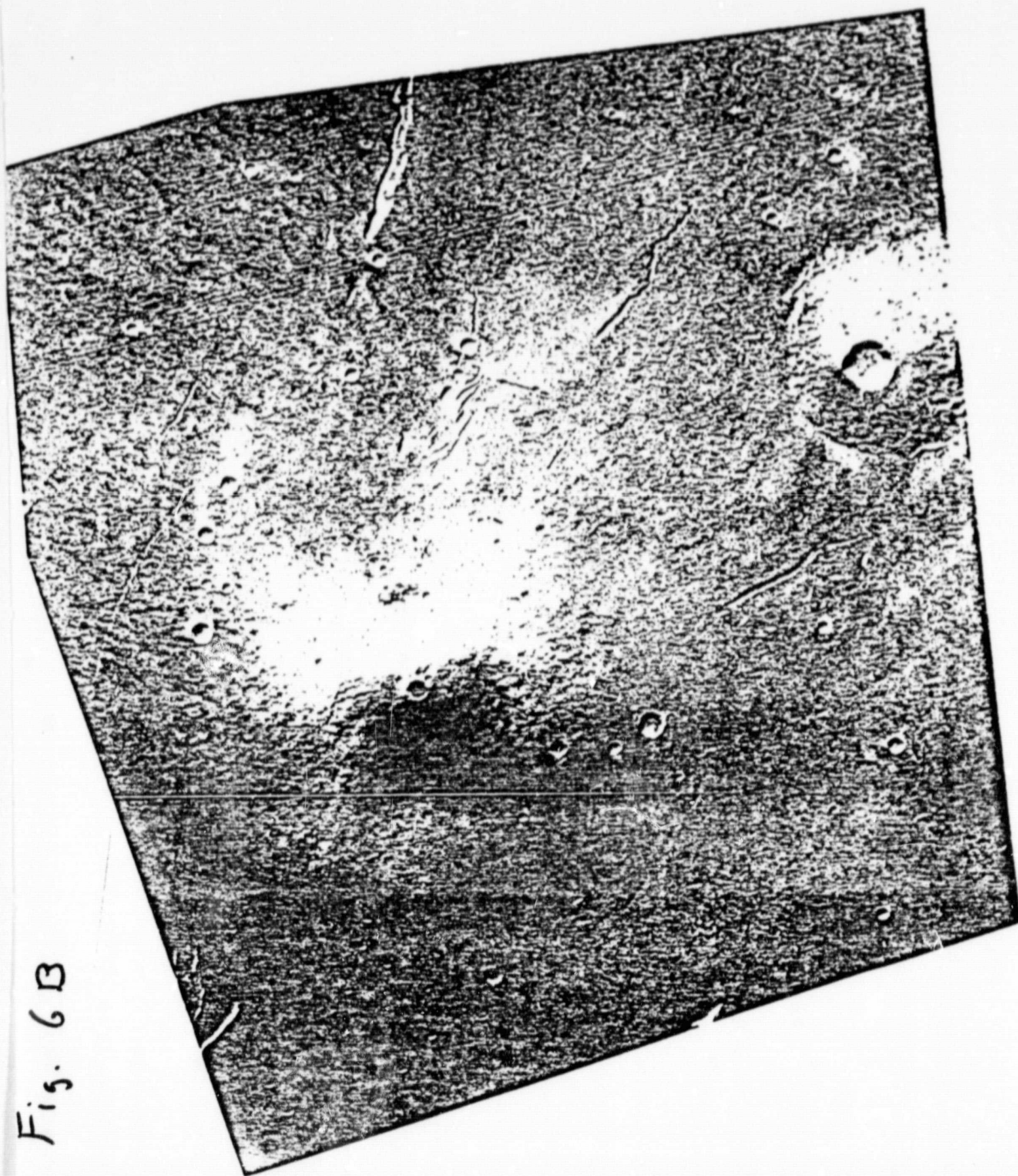
ORIGINAL PAGE IS
OF POOR QUALITY

Fig. 5B



Fig. 6A

Fig. 6B



ORIGINAL PAGE IN
U.S. AIR FORCE
ARCHIVE

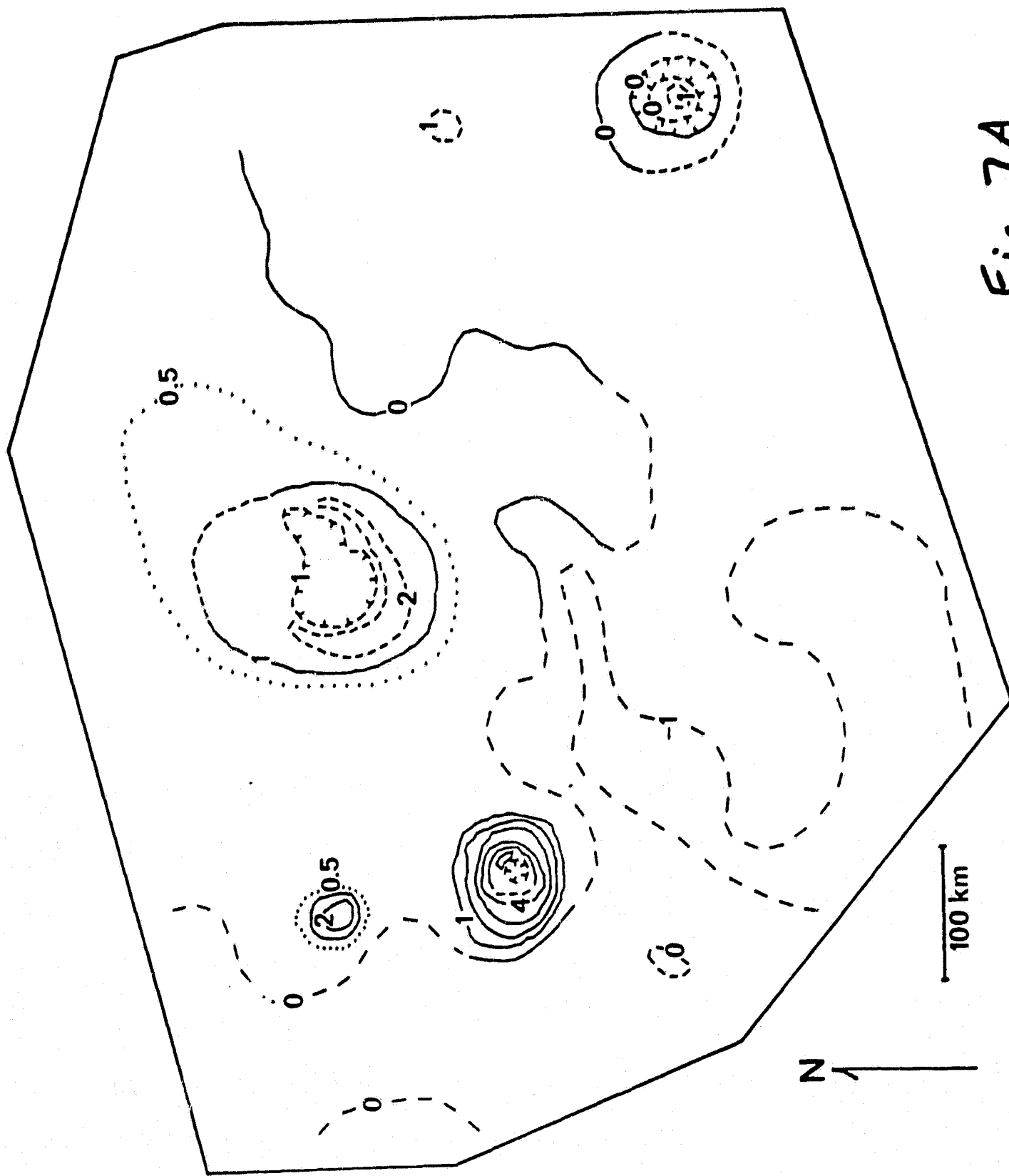
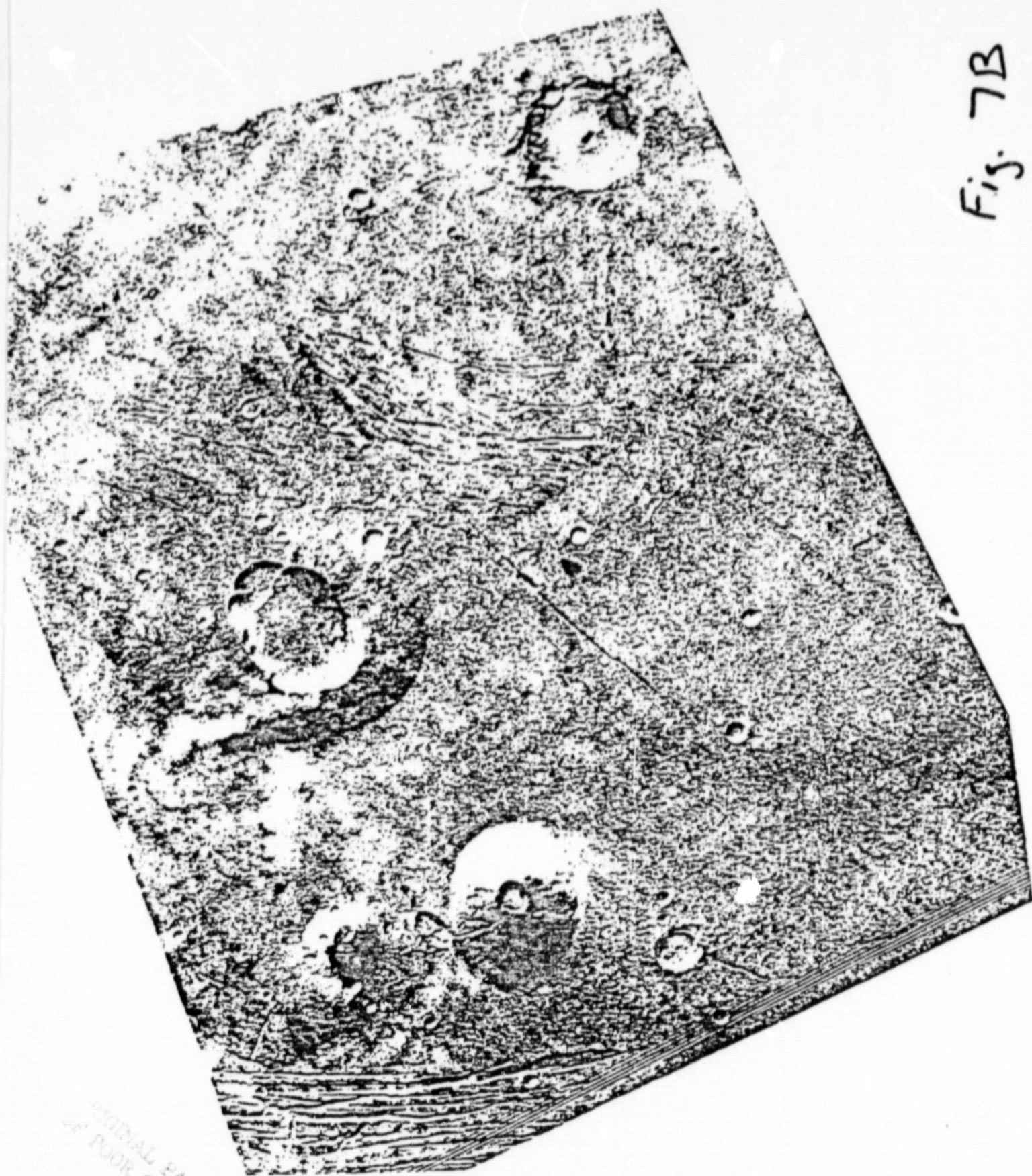


Fig. 7A

Fig. 7B



ORIGINAL PAGE IS
OF POOR QUALITY

APPENDIX A: TOPOGRAPHY OF OLYMPUS MONS

Because of its spectacular relief and bulk, Olympus Mons has been the object of several topographic studies using imaging data. All previous studies used Mariner 9 imaging, and, for the most part, they agree with the topographic map presented in this paper. Blasius (1973) used relief displacements due to topography in a single stereo pair, Wu et al. (1973) used an AP/C analytical plotter to compile a contour map from the same stereo pair, Whitehead (1974) used high oblique photography of the volcano and the limb of Mars in conjunction with latitude and longitude coordinates of surface features derived by Davies and Arthur (1973), Davies (1974) applied his geodetic triangulation technique with aerocentric radius allowed to vary, and Arthur (1976) applied several different approaches to elevation estimation using image coordinates of Davies (1974). The first two studies utilized data for only a fraction of the shield, so detailed comparison with the map presented in this paper is hampered.

The results of Whitehead (1974), Davies (1974), and Arthur (1976) are similar but the error analysis of the last seems most complete. After separately deriving the topography of Olympus Mons using oblique photography, near vertical photography, and spacecraft navigation data, Arthur (1976) arrives at a "combined" solution to which he attaches the smallest esti-

mated standard errors, ± 3.5 km in relative elevation. We present here a comparison of point feature relative elevations from these three papers with elevations taken from our map of Olympus Mons (Figure 5A).

In Table A1 are listed a sample of point feature relative elevations taken from the three geodetic studies and our elevation estimates based on the Figure 5A map of Olympus Mons and the index of feature measurements, Figure 3B. Confidence limits given by the authors are also shown along with explanatory notes. Figure A1 is an index of the locations of the point features. In Figure A2 the relative elevations are compared by means of point-to-point plots. Bearing in mind the estimated errors of ± 3.5 km and ± 0.5 km of Arthur's (1976) and our data, respectively, the agreement is remarkably good. Only for the points 1608 and 1609 is there an indication of a possible discrepancy. These points lie in an area on the west flank of Olympus Mons where imaged features are all of low contrast. Our map indicates uncertainty in elevation measurements across much of this area.

The Whitehead (1974) and Davies (1974) data are similarly consistent with our results. Their estimated errors are significantly smaller than those of Arthur (1976), but the error analyses are incomplete (Table A1).

REFERENCES (Appendix)

- Arthur, D.W.G., 1976, The Nix Olympica Problem: An Exercise in Planetary Photogrammetry, Photogrammetric Record, 8, 617-630.
- Blasius, K.R., 1973, A Study of Martian Topography by Analytic Photogrammetry, J. Geophys. Res., 78, 4411-4423.
- Davies, M.E., and Arthur, D.W.G., 1973, Martian Surface Coordinates, J. Geophys. Res., 78, 4355.
- Davies, M.E., 1974, Photogrammetric Measurements of Olympus Mons on Mars, Icarus, 21, 230-236.
- Whitehead, A.B., 1974, The Elevation of Olympus Mons from Limb Photography, Icarus, 22, 189-196.
- Wu, S.S.C., Schafer, F.J., Nakata, G.M., Jordan, R., and Blasius, K.R., 1973, Photogrammetric Evaluation of Mariner 9 Photography, J. Geophys. Res., 78, 4405-4423.

FIGURE CAPTIONS (Appendix A)

- A1. Index of locations of point features having elevations determined by Arthur (1976), Davies (1974), and Whitehead (1974) for comparison with new topographic data of this paper.
- A2. Point-to-point comparison of relative elevation data for Olympus Mons. The index numbers indicate features with positions shown in Figure A1.

TABLE A1: LOCAL TOPOGRAPHY OF OLYMPUS MONS
COMPARISON OF FOUR ANALYSES

Relative Elevation and Estimated Error

Point	Whitehead (1974) ^{2.}	Davies (1974) ^{3.}	Arthur (1976)	This Paper ^{4.}
405	22.1 \pm 2	19.4 \pm 1.9	19.6 \pm 3.5	17.5 \pm 0.5
406	--	4.8 \pm 2.0	5.4 \pm 3.5	6.5 \pm 0.5
407	--	--	9.1 \pm 3.5	7.5 \pm 1.0
1601	- 0.3 \pm 1	-0.8 \pm 1.6	-1.8 \pm 3.5	-2.0 \pm 0.5
1602	4.3 \pm 1	3.5 \pm 1.5	2.6 \pm 3.5	3.5 \pm 0.5
1603	21.5 \pm 1	20.2 \pm 1.3	20.2 \pm 3.5	21.0 \pm 0.5
1604	6.6 \pm 1	5.0 \pm 1.9	4.6 \pm 3.5	3.5 \pm 0.5
1605	-0.2 \pm 1	1.0 \pm 1.3	-0.1 \pm 3.5	2.0 \pm 0.5
1606 ^{1.}	20.0 \pm 1	20.0 \pm 1.4	20.0 \pm 3.5	20.0 \pm 0.5
1607	--	7.2 \pm 2.0	7.7 \pm 3.5	6.5 \pm 0.5
1608	11.1 \pm 2	--	6.1 \pm 3.5	11.5 \pm 1.0
1609	--	--	7.4 \pm 3.5	13.0 \pm 2.0

1. relative elevation of point 1606 was arbitrarily set to 20 km to allow comparison of data sets
2. estimate of error includes only the identification of conjugate features in images and on controlled mosaics; not estimated is the effect of uncertainty in mosaic geodetic control by Davies and Arthur (1973)
3. the standard errors cited here represent residual discrepancies between image coordinates and the best fit geodetic model, not a covariance analysis for systematic errors
4. estimated errors larger than the nominal \pm 0.5 km cited for the Figure 5A map are due to uncertain identification of a point feature because a digital area matching algorithm was used by us on exceptionally distant interpolation between measured features was required (see Fig. 3B).

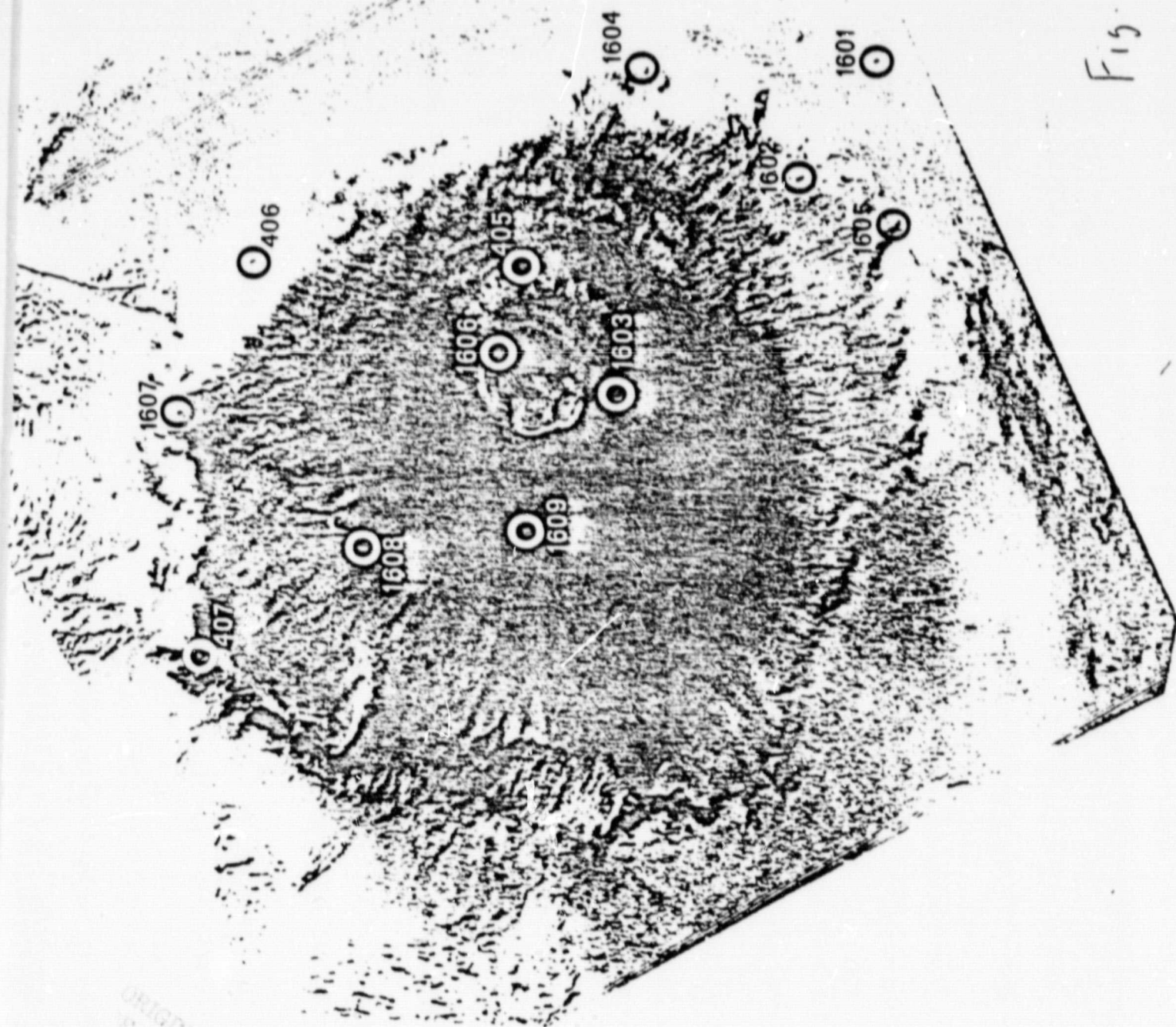


Fig. A1

ORIGINAL PAGE IS
OF POOR QUALITY

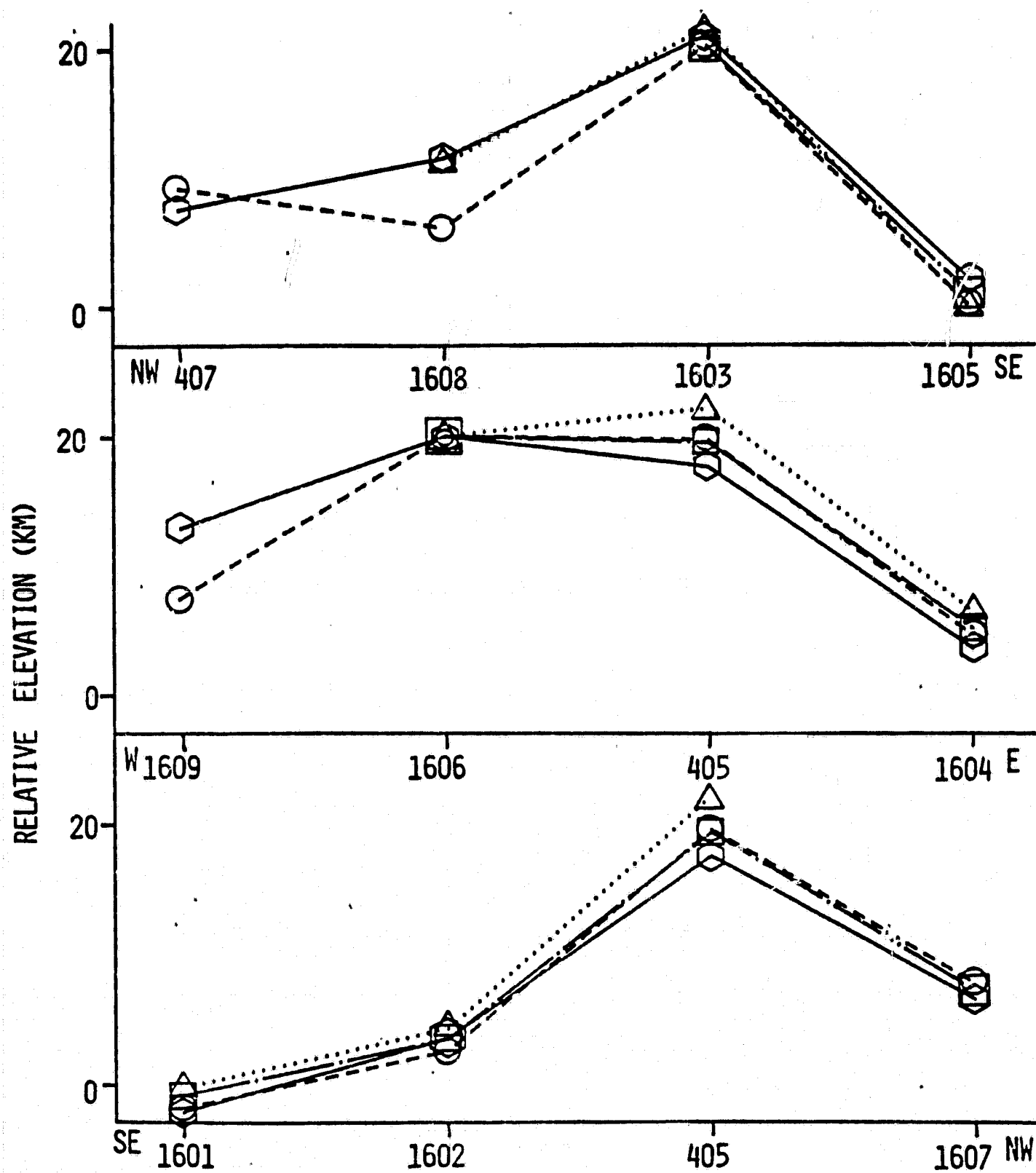


FIGURE I.D. NUMBER

..... Δ WHITEHEAD, 1974 ----- \circ ARTHUR, 1976
 — \square DAVIES, 1974 — \diamond THIS PAPER

Fig. A2

APPENDIX 2.1

DATA BASE DEVELOPED IN TASK 2

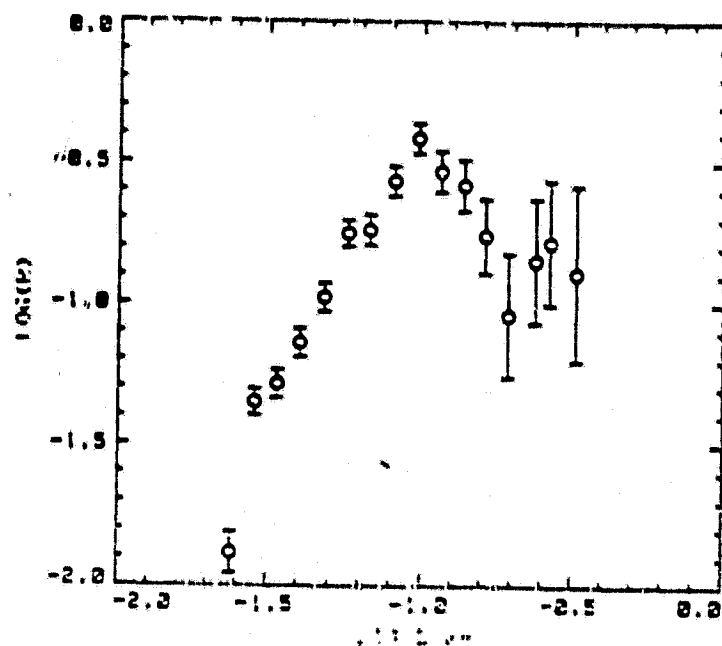
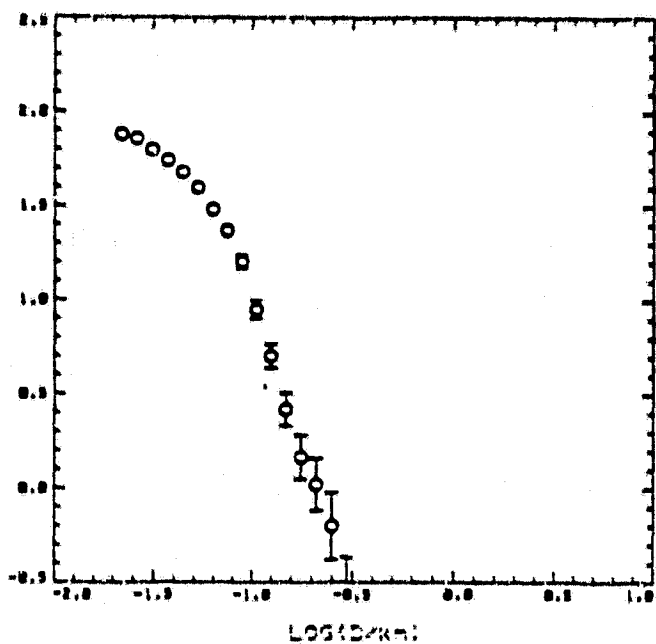
Overlays were prepared for 20 Lunar Orbiter photographs, with the craters classified crudely into 4 degradation classes. The photographs chosen are listed below (H \equiv high resolution; M \equiv medium resolution; E \equiv enlargement.) The numeral in parentheses is the number of craters counted in that photograph.

II-88-H2	(544)	V-183-M	(227)
II-88-H2-E	(292)	V-190-H3	(1378)
II-88-M	(914)	V-190-H3-E	(1007)
III-173-M	(10035)	V-191-H3	(1237)
III-174-H2	(1080)	V-191-M	(343)
III-174-H2-E	(521)	V-214-H1	(2318)
V-72-H	(216)	V-214-H1-E	(758)
V-74-M	(343)	V-214-H2	(2258)
V-183-H2	(2847)	V-214-H2-E	(674)
V-183-H2-E	(1452)	V-215-M	(171)

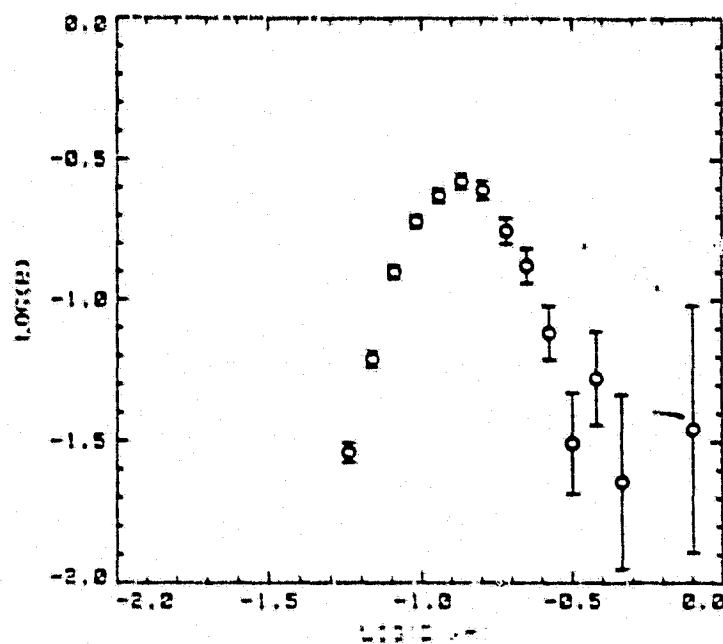
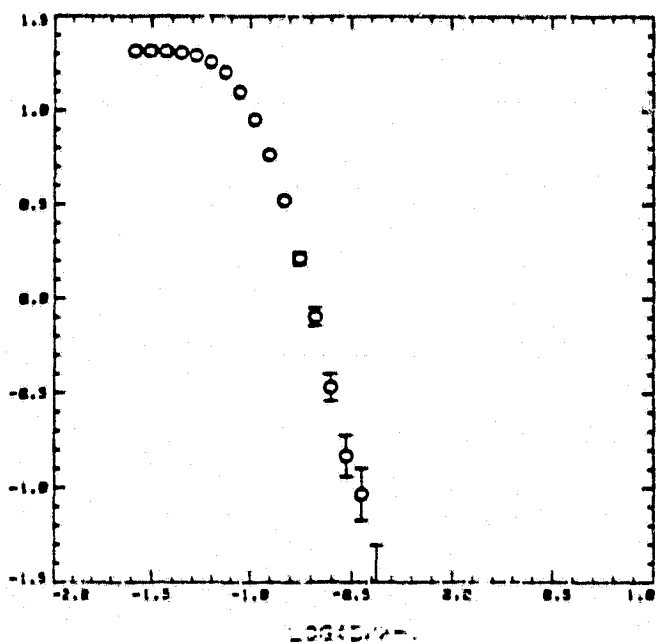
These 19,615 craters were then digitized by position, diameter, and morphological class with a Numonics 1224 digitizer on line to a HP9845S minicomputer. The computer drew four-color plots to compare with the original overlays. After the data files were edited to eliminate errors, cumulative and relative distributions were plotted for each of the four

morphological types and the total. Thus, ten plots were prepared for each photograph, making 200 altogether. In the following figure (D1) we give examples of these plots for all the craters in two lunar orbiter photographs. On the left hand side are exhibited the cumulative number density and on the right the unitless relative number density,

$$R = nD^3/A(D_{\max} - D_{\min}).$$



a) 758 total craters on V-214-H1-E, area = 9.5 km^2 .



b) 2258 total craters V-214-H2; area = 109 km^2 .

APPENDIX 2.2

SUB-KILOMETER LUNAR CRATERS: ORIGINS, AGES, PROCESSES OF DEGRADATION, AND IMPLICATIONS FOR MARE BASALT PETROGENESIS. Clark R. Chapman¹, Jayne C. Aubele^{1,2}, Wm. James Roberts³, and James A. Cutts³, (¹Planetary Science Institute, 2030 E. Speedway, Tucson, AZ 85719; ²Dept. Planetary Science, Univ. of Arizona, Tucson AZ 85721; ³Planetary Science Institute, 283 S. Lake Ave., Pasadena, CA 91101)

The size distributions of sub-kilometer lunar craters generally have been interpreted during the past decade to be the product of impact cratering and gardening in the regolith. One important application of this interpretation has been the assignment of relative ages to lunar mare units using a crater morphological parameter called D_L (1). Correlations of such D_L ages with mare basalt compositions inferred from spectrophotometry have been used as constraints for petrogenetic and thermal models for the evolution of mare basalt source regions with time. Such interpretations based on D_L ages would be wrong, however, if many sub-km lunar craters were of endogenic rather than impact origin, as has been proposed by a minority of workers (2-7).

Motivated by this important problem in basaltic volcanism, we embarked on a new project to study small crater populations in several carefully selected lunar mare regions, representative of both red and blue basalt types with both "young" and "old" D_L ages. The methodology employed is the same as applied to a variety of other lunar regions by Chapman et al (4). Craters of diameter 20m to 2km were counted and classified into 4 morphological classes. In order to correct for systematic classification and measurement biases between the present study and earlier ones (4 and 7), regions common to those earlier studies were also measured again.

The new crater size distributions show many of the same anomalous features previously reported that have seemed incompatible with a simple model of impact cratering and equilibrium degradation and obliteration by the cratering process. In particular our "young blue" units show an excess of ~100m diameter (largely degraded) craters compared with both the "old red" and "old blue" provinces studied; the excesses approach factors of 2 to 5 respectively and violate our intuitive expectation that younger units should always have the same number or fewer craters than older units. Most of the regions we have measured share most of the characteristics previously ascribed to the "Imbrium" or "Alphonsus" population types described by Chapman et al (4) (called Types I and III by Schultz et al 7).

Preliminary examination of our size-frequency plots show few cases where even small segments of the distributions approach the -2 cumulative distribution slope characteristic of classical equilibrium. There are numerous bumps and dips in the distributions that do not always seem to be compatible with the two-layer differential erosion process described by Schultz et al (7). But an elaboration of that model permits us to explain most of the major features of these distributions without requiring an ad hoc endogenic component to the population. Schultz et al pointed out that differential erosion and degradation of larger craters formed in bedrock and smaller craters formed wholly in regolith would yield offset equilibrium populations approximately as observed. We point out that, in addition, differences in energy/diameter scaling relations in the regolith and bedrock substantially modify the production function (see Fig. 9 left in Ref. 4), which is manifested in the equilibrium population of craters

SUB-KILOMETER LUNAR CRATERS

Chapman, C. R. et al

in a manner not envisioned by Schultz et al. Together, the two scaling effects produce a complicated pattern of frequency relations for craters of different morphological classes (and for all classes together) similar to those observed. In particular, our two-layer impact model yields the steep distribution slope observed for some populations at sizes $>300\text{m}$, ascribed by Schultz et al. to a superposed population of non-impact craters.

Included in our interpretation are expectations that craters with dimensions comparable to the regolith depth may be formed with initially "degraded" morphology. Furthermore, we expect the equilibrium percentages of craters in the several classes (and the percentage of geometric saturation for total craters) to vary with size due to different degradation processes that operate at different scales. Preliminary examination suggests our data are compatible with these expectations.

While we believe our results diminish the requirements for a substantial endogenic crater population, there remain some puzzling features of our data and other previously published distributions. In addition, we believe that it remains difficult to understand the preservation of the small primary flow features (ring moats, etc.) described by Schultz et al (6) if crater degradation is proceeding at the rates implied by our present model. And there is clear evidence that endogenic craters do, in fact, exist in at least some lunar localities (e.g. those craters arranged in chains).

But on balance we believe that the case for predominant impact cratering as the origin of the small lunar crater populations is strengthened by these considerations. In view of these results, we believe it likely that a crater morphological parameter such as D_L may reflect relative ages of lunar provinces and thus ultimately be useful for establishing the chronology of basalt emplacement. On the otherhand, it remains to be evaluated to what degree modifications of the application of the D_L criterion will be required to take account of the more complicated, target-dependent cratering and erosive processes implied by our interpretation and the associated work of Schultz, Greeley, and Gault.

References: (1) Boyce, J.M. (1976) Proc. Lunar Sci. Conf. 7th, 2717-2728. (2) Kuiper, G.P., Strom, R.G., LePoole, R.S. (1966) Ranger 8 and 9 Part 2, JPL Tech. Rept. 32-800, 35-248. (3) Chapman, C.R. (1968) Icarus 8, 1-22. (4) Chapman, C.R., Mosher, J.A., and Simmons, G. (1974) J. Geophys. Res. 75, 1445-1446. (5) Fielder, G., Fryer, R.J., Titulaer, C., Herring, A.K., and Wise, B. (1972) Phil. Trans. Roy. Soc. London 271, 361-409. (6) Schultz, P.H., Greeley, R., and Gault, D.E. (1976) Proc. Lunar Sci. Conf. 7th, 985-1003. (7) Schultz, P.H., Greeley, R., and Gault, D.E. (1977) Lunar Science VIII 858-860.